Fast Tensor Needlet Transforms for Tangent Vector Fields on the Sphere

Ming Li, Jialin Chen, Philip Broadbridge, Andriy Olenko, Yu Guang Wang†

Abstract

This paper constructs a semi-discrete tight frame of tensor needlets associated with a quadrature rule for tangent vector fields on the two-dimensional sphere. Fast algorithms for needlet transforms (fast needlet transforms), which include the decomposition and reconstruction of the needlet coefficients between different levels, are given. The fast needlet transforms have linear computational complexity since they rely on the developed fast Fourier transforms for vector spherical harmonics. Numerical examples for the simulated and real data demonstrate the efficiency of the proposed methodology.

Index Terms

Tangent vector field, Tensor needlets, Tight frames, Spherical harmonics, FFTs

I. Introduction

Tangent vector fields on the sphere appear in many real-world applications, such as geophysics, astrophysics, and environmental sciences, in which wind and oceanic currents, gravity, electric and magnetic fields are some of the most well-studied examples [1]–[5]. Numerous processes studied in geosciences, planetary science and cosmology exhibit relatively small changes in their vertical(radial) direction compared to surface(tangential) directions. In many application the vertical component can be neglected and only tangential components are of main interest. Tangent vector fields also can be an important model and tool to further investigate evolutions of systems described by partial differential equation on the sphere, see [2], [6] and references therein.

It is known that each tangent vector field can be decomposed into two components: divergent-free and curl-free, and each part may provide some important physical insight in specific changes of vector fields. Compared with the available theory and learning tools for scalar fields on the sphere and other manifolds, modelling tangent vector fields has been less studied, which was the main motivation of this research.

M. Li is with the Department of Educational Technology, Zhejiang Normal University, Jinhua 321004, China (email:mingli@zjnu.edu.cn)

J. Chen is with Institute of Natural Sciences, and School of Mathematical Sciences, Shanghai Jiao Tong University, Shanghai, China (email:sjtuchenjl@sjtu.edu.cn)

P. Broadbridge and A. Olenko are with the School of Engineering and Mathematical Sciences, La Trobe University, Victoria 3086, Australia (e-mail: p.broadbridge@latrobe.edu.au; a.olenko@latrobe.edu.au)

Y. G. Wang is with Institute of Natural Sciences, and School of Mathematical Sciences, Key Laboratory of Scientific and Engineering Computing of Ministry of Education (MOE-LSC), Shanghai Jiao Tong University, Shanghai, China, and also with the School of Mathematics and Statistics, The University of New South Wales, Sydney 2052, Australia (email:yuguang.wang@sjtu.edu.cn)

† Corresponding author

Several techniques have been developed for vector field approximation on the sphere. In the early 1980's, Wahba [7] used vector spherical harmonics (VSH) to construct the approximation of the tangent vector field. Freeden and Gervens [8] considered a similar approximation technique using vector spherical splines. They introduced positive definite kernels for fitting and decomposing a field using spherical basis functions (SBFs). The Geomathematics Group at the University of Kaiserslautern also provided several kernel based approaches [1], [9]. Publications [10], [11] investigated the approximation of the stream function (divergence-free part) and velocity potential (curl-free part) of the field, which however relies on the computation of the divergence and vorticity of the field. In [12], Fuselier and Wright studied the spherical basis function interpolation and approximation for tangent vector fields on the sphere, providing both theoretical and simulation verifications on the stability and error estimations. However, a common shortcoming for the interpolant-based approximation is that solving a linear system (to find the optimal coefficient vectors) can be computationally expensive when the set of scattered data points is quite large.

The multiresolution analysis is well developed to deal with sparse high-dimensional data in the Euclidean space $\mathbb{R}^d$. It allows fast algorithm implementations for building the approximators. Multiscale representation systems in $\mathbb{R}^d$ including wavelets, framelets, curvelets, shearlets, etc., have been well-developed and widely used, see e.g. [13]–[19]. The core of the classical framelet (and wavelet) construction relies on the extension principles such as unitary extension principle (UEP) [20], oblique extension principle (OEP) and mixed extension principle (MEP) [21]. The extension principles associate framelet systems with filter banks, which enables fast algorithmic realizations for the framelet transforms and applications, see e.g. [18], [21], [22]. The fast algorithms include the filter bank decomposition and reconstruction of a representation system which uses the convolution and the fast Fourier transforms (FFTs) and achieve computational complexity in proportion to the size of the input data (up to a log factor). However, multiscale representation systems on the sphere and their corresponding fast algorithm implementation are less studied. Wang and Zhuang [23] constructed a tight framelet system on a mainfold by means of orthogonal polynomials, localized kernels and affine systems. It was used to develop fast algorithmic realizations for the multi-level framelet filter bank transforms using discrete FFTs on compact Riemannian manifolds. Similar approaches can be seen in Fischer, Mhaskar and Prestin in [24], [25]. Coifman, Maggioni, Mhaskar and Dong [26]–[29] considered more general cases, for which diffusion wavelets, diffusion polynomial frames and wavelet tight frames on manifolds and graphs were constructed. These frameworks have been well developed for scalar fields, but the case of vector fields on the sphere is little studied.

In this paper, we study multiresolution analysis for tangent vector fields on the sphere. Using the framework in [23] and fine properties of vector spherical harmonics, we first construct the tight frame of continuous tensor needlets and then semi-discrete ones. The approach is based on discretization of the continuous systems using a sequence of polynomial-exact quadrature rules on the sphere. We give the theoretical results on the equivalence conditions for a sequence of (continuous and semi-discrete) tensor needlets to be a sequence of tight frames on $\mathbf{L}_2(\mathbb{S}^2)$. These results offer tools to construct tensor needlet transforms and filter banks for a tight tensor needlet system. Then, we detail the multi-level tensor needlet transforms that include the decomposition and reconstruction. Namely, we decompose tensor needlet coefficients into a coarse scale approximation coefficient sequence (low-pass) together

with multiple coarse scale detail coefficient sequences (high-pass) and reconstruct from the coarse scale approximation and details to fine scales. In particular, downsampling and upsampling operations are used in the decomposition and reconstruction, while (discrete) convolutions with filters in the filter bank are employed in both. Using the recently developed FFTs for vector spherical harmonic (FaVeST) in [30], we can speed up the decomposition and reconstruction by implementing discrete Fourier transforms in the convolutional operations. It leads to fast tensor needlet transform (FNT) algorithms. Numerical simulations, including simulated vector fields with characteristics similar to those of atmospheric wind fields and real-world case study of climatological wind field, demonstrate the efficiency of our proposed algorithms.

The main contributions of the paper are:

- The construction of tight continuous and semi-discrete tensor needlet systems with rigorous theoretical analysis of their tightness;
- The development of fast tensor needlet transforms with nearly linear computational complexity and low redundancy rate based on FFTs for vector spherical harmonic transforms (FaVeST);
- An extension of results in [23] to the case of tangent vector fields on the sphere;
- Detailed numerical studies that demonstrate that the developed fast algorithms work favourably on modelling tangent vector fields on the sphere, and also indicate a good potential on vectorial approximation via localized tight frames of tensor needlets.

The paper is organized as follows. In Section II we introduce the necessary background and notation. The construction of tight frames of tensor needlets (for both continuous and discrete case) are given in detail in Section III. Section IV details the algorithmic implementations of fast needlet transforms. Numerical studies to validate the obtained results are given in Section V.

II. Preliminaries

Let $\mathbb{C}^3$ be the 3-dimensional complex coordinate space. In the following, the elements of $\mathbb{C}^3$ are column vectors. For $\boldsymbol{x} \in \mathbb{C}^3$, let the row vector $\boldsymbol{x}^T$ be the transpose of $\boldsymbol{x}$ and $\overline{\boldsymbol{x}}$ is the complex conjugate to $\boldsymbol{x}$. The inner product of two vectors $\boldsymbol{x}$ and $\boldsymbol{y}$ in $\mathbb{C}^3$ is $\boldsymbol{x} \cdot \boldsymbol{y} = \sum_{i=1}^3 x_i \overline{y_i}$, where x_i, y_i are components of $\boldsymbol{x}$ and $\boldsymbol{y}$. The (Euclidean) ℓ_2 norm of $\boldsymbol{x}$ is $|\boldsymbol{x}| = \sqrt{\boldsymbol{x} \cdot \boldsymbol{x}}$. The tensor product for two vectors $\boldsymbol{x}$ and $\boldsymbol{y}$ in $\mathbb{C}^3$ is a matrix $\boldsymbol{x} \otimes \boldsymbol{y}$ such that

$$(\boldsymbol{x} \otimes \boldsymbol{y})_{i,j} = x_i \overline{y_j}.$$

$\boldsymbol{x} \otimes \boldsymbol{y} = \boldsymbol{x}\overline{\boldsymbol{y}}^T$ is the matrix product of $\boldsymbol{x}$ with the transpose of $\boldsymbol{y}$.

A. Function spaces and vector spherical harmonics

Let $\mathbb{S}^2$ be the unit sphere in $\mathbb{R}^3$. A $\mathbb{C}^3$-valued function (defined on $\mathbb{S}^2$) is called a *vector field* on $\mathbb{S}^2$. For a vector field $\boldsymbol{f}$ on $\mathbb{S}^2$, the *normal vector field* and *tangent vector field* for $\boldsymbol{f}$ are

$$\boldsymbol{f}_{\mathrm{nor}}(\boldsymbol{x}) := (\boldsymbol{f} \cdot \boldsymbol{x})\boldsymbol{x}, \quad \boldsymbol{f}_{\tan}(\boldsymbol{x}) := \boldsymbol{f} - \boldsymbol{f}_{\mathrm{nor}},$$

where $\boldsymbol{x} \in \mathbb{S}^2$. A vector field $\boldsymbol{f}$ is called *tangent vector field* if $\boldsymbol{f} = \boldsymbol{f}_{\tan}$, i.e., $\boldsymbol{f}_{\mathrm{nor}}(\boldsymbol{x}) \equiv 0$ on $\mathbb{S}^2$. In this paper, we study the tangent vector field.

Let $\mathbf{L}_2(\mathbb{S}^2)$ be the L_2 space of tangent vector fields on $\mathbb{S}^2$ with the inner product

$$\langle \boldsymbol{f}, \boldsymbol{g} \rangle := \langle \boldsymbol{f}, \boldsymbol{g} \rangle_{\mathbf{L}_2(\mathbb{S}^2)} := \int_{\mathbb{S}^2} \boldsymbol{f}(\boldsymbol{x}) \cdot \boldsymbol{g}(\boldsymbol{x}) \, \mathrm{d}\sigma(\boldsymbol{x}), \quad \boldsymbol{f}, \boldsymbol{g} \in \mathbf{L}_2(\mathbb{S}^2)$$

and the induced finite L_2 norm $\|\boldsymbol{f}\|_{\mathbf{L}_2(\mathbb{S}^2)} := \sqrt{\langle \boldsymbol{f}, \boldsymbol{f} \rangle}$. For a vector field $\boldsymbol{f} = (f_1, f_2, f_3)^T \in \mathbf{L}_2(\mathbb{S}^2)$, the integral $\int_{\mathbb{S}^2} \boldsymbol{f}(\boldsymbol{x}) \mathrm{d}\sigma(\boldsymbol{x})$ of $\boldsymbol{f}$ on $\mathbb{S}^2$ denotes the vector of componentwise integrals $(\int_{\mathbb{S}^2} f_1(\boldsymbol{x}) \mathrm{d}\sigma(\boldsymbol{x}), \int_{\mathbb{S}^2} f_2(\boldsymbol{x}) \mathrm{d}\sigma(\boldsymbol{x}), \int_{\mathbb{S}^2}$

A $\mathbb{C}^{3\times 3}$-valued *tensor field* $\mathbf{u}$ on $\mathbb{S}^2$ is a $\mathbb{C}^{3\times 3}$-valued function on $\mathbb{S}^2$. Suppose that each column of $\mathbb{C}^{3\times 3}$-valued tensor field $\boldsymbol{u}$ is a vector field in $\mathbf{L}_2(\mathbb{S}^2)$, that is, $\mathbf{u} = (\boldsymbol{u}_1, \boldsymbol{u}_2, \boldsymbol{u}_3)$ and $\boldsymbol{u}_i \in \mathbf{L}_2(\mathbb{S}^2)$, $i = 1, 2, 3$. For $\boldsymbol{f} \in \mathbf{L}_2(\mathbb{S}^2)$, we define the "inner product" between $\boldsymbol{f}$ and $\mathbf{u}$ by

$$\langle \boldsymbol{f}, \mathbf{u} \rangle := \Big(\langle \boldsymbol{f}, \boldsymbol{u}_1 \rangle, \quad \langle \boldsymbol{f}, \boldsymbol{u}_2 \rangle, \quad \langle \boldsymbol{f}, \boldsymbol{u}_3 \rangle \Big).$$

For $\boldsymbol{f}, \boldsymbol{g}, \boldsymbol{h} \in \mathbf{L}_2(\mathbb{S}^2)$ and $\boldsymbol{y} \in \mathbb{S}^2$,

$$\langle \boldsymbol{f}, \boldsymbol{g} \otimes \boldsymbol{h}(\boldsymbol{y}) \rangle = \langle \boldsymbol{f}, \boldsymbol{g} \rangle \, \boldsymbol{h}(\boldsymbol{y})^T, \quad \langle \boldsymbol{h}(\boldsymbol{y}) \otimes \boldsymbol{g}, \boldsymbol{f} \rangle = \boldsymbol{h}(\boldsymbol{y}) \, \langle \overline{\boldsymbol{g}}, \boldsymbol{f} \rangle = \big\langle \overline{\boldsymbol{f}}, \boldsymbol{g} \big\rangle \, \boldsymbol{h}(\boldsymbol{y}),$$

where $\boldsymbol{h}(\boldsymbol{y})^T := (\boldsymbol{h}(\boldsymbol{y}))^T$ for simplicity. We will use this notation in the paper if no confusion arises.

Let Δ^* be the Laplace-Beltrami operator on $\mathbb{S}^2$. Complex-valued spherical harmonics $Y_{\ell,m}$, $\ell \in \mathbb{N}_0, m = -\ell, \ldots, \ell$, are eigenfunctions of Δ^* with eigenvalues $\lambda_\ell := \ell(\ell+1)$ satisfying

$$\Delta^* \, Y_{\ell,m} = \lambda_\ell \, Y_{\ell,m}.$$

Let ∇ be the gradient on $\mathbb{R}^3$. The *surface-gradient* on $\mathbb{S}^2$ is defined as $\nabla_* := P_x \nabla$ with the matrix $P_{\boldsymbol{x}} := I - \boldsymbol{x}\boldsymbol{x}^T$, where I is the identity matrix. The *surface-curl* on $\mathbb{S}^2$ is $\mathbf{L} = Q_x \nabla$ with the matrix

$$Q_{\boldsymbol{x}} := \begin{pmatrix} 0 & -x_3 & x_2 \\ x_3 & 0 & -x_1 \\ -x_2 & x_1 & 0 \end{pmatrix}.$$

Then, it holds $\nabla_* \cdot \nabla_* = \mathbf{L} \cdot \mathbf{L} = -\Delta^*$.

The *divergence-free vector spherical harmonics* are

$$\mathbf{y}_{\ell,m} = \mathbf{L} Y_{\ell,m} / \sqrt{\lambda_\ell}, \quad \ell \geq 1.$$

The *curl-free vector spherical harmonics* are

$$\mathbf{z}_{\ell,m} = \nabla_* Y_{\ell,m} / \sqrt{\lambda_\ell}, \quad \ell \geq 1.$$

The set $\{(\mathbf{y}_{\ell,m}, \mathbf{z}_{\ell,m}) : \ell \geq 1, m = -\ell, \ldots, \ell\}$ forms an orthonomal basis of $\mathbf{L}_2(\mathbb{S}^2)$, see e.g. [1], [12].

Let $\widehat{\boldsymbol{f}}_{\ell m} := \langle \boldsymbol{f}, \mathbf{y}_{\ell,m} \rangle$ and $\widetilde{\boldsymbol{f}}_{\ell m} := \langle \boldsymbol{f}, \mathbf{z}_{\ell,m} \rangle$ be the (divergence-free and curl-free) Fourier coefficients for $\boldsymbol{f} \in \mathbf{L}_2(\mathbb{S}^2)$. For $\boldsymbol{f} \in \mathbf{L}_2(\mathbb{S}^2)$, it holds

$$\boldsymbol{f} = \sum_{\ell=1}^{\infty} \sum_{m=-\ell}^{\ell} \Big(\widehat{\boldsymbol{f}}_{\ell m} \, \mathbf{y}_{\ell,m} + \widetilde{\boldsymbol{f}}_{\ell m} \, \mathbf{z}_{\ell,m} \Big)$$

in $\mathbf{L}_2(\mathbb{S}^2)$ space.

For $\ell \geq 1$, the divergence-free and curl-free *Legendre rank-2 kernels* of degree ℓ are the tensor fields

$$\mathbf{p}_\ell(\boldsymbol{x}, \boldsymbol{y}) = \frac{2\ell+1}{4\pi\lambda_\ell} (\nabla_*)_{\boldsymbol{x}} \otimes (\nabla_*)_{\boldsymbol{y}} P_\ell(\boldsymbol{x} \cdot \boldsymbol{y}), \quad \mathbf{q}_\ell(\boldsymbol{x}, \boldsymbol{y}) = \frac{2\ell+1}{4\pi\lambda_\ell} \mathbf{L}_{\boldsymbol{x}} \otimes \mathbf{L}_{\boldsymbol{y}} P_\ell(\boldsymbol{x} \cdot \boldsymbol{y}), \quad \boldsymbol{x}, \boldsymbol{y} \in \mathbb{S}^2.$$

For vector spherical harmonics and Legendre rank-2 kernels, the following addition theorem holds

$$\sum_{m=-\ell}^{\ell} \mathbf{y}_{\ell,m}(\boldsymbol{x}) \otimes \mathbf{y}_{\ell,m}(\boldsymbol{y}) = \mathbf{p}_\ell(\boldsymbol{x},\boldsymbol{y}), \qquad \sum_{m=-\ell}^{\ell} \mathbf{z}_{\ell,m}(\boldsymbol{x}) \otimes \mathbf{z}_{\ell,m}(\boldsymbol{y}) = \mathbf{q}_\ell(\boldsymbol{x},\boldsymbol{y})$$

for $\ell \geq 1$ and $\boldsymbol{x}, \boldsymbol{y} \in \mathbb{S}^2$, see [1, Theorem 5.3].

III. Tight Frame of Tensor Needlets

In this section, we construct a localized tight frame on vector fields Z that are defined on $\mathbb{S}^2$ and taking values in $\mathbb{R}^d$. Here we inherit the notation and concepts of [23], [31]–[33].

Let $\mathbb{L}_2(\mathbb{R})$ be the space of complex-valued square-integrable functions on $\mathbb{R}$, and let $\ell_2(\mathbb{Z})$ be a space of square-summable sequences on $\mathbb{Z}$. The Fourier transform of $\phi \in \mathbb{L}_2(\mathbb{R})$ is $\widehat{\phi}(\xi) := \int_{\mathbb{R}} \phi(x) e^{-2\pi i x\xi}\, \mathrm{d}\xi$, $\xi \in \mathbb{R}$. The Fourier series for $h \in \ell_2(\mathbb{Z})$ is $\widehat{h} := \sum_{k\in\mathbb{Z}} h_k e^{-2\pi i k\xi}$, $\xi \in \mathbb{R}$.

Let

$$\digamma := \{\alpha, \beta^1, \ldots, \beta^r\} \tag{III.1}$$

be a set of functions in $\mathbb{L}_2(\mathbb{R})$. We call $\digamma$ a set of *generating functions* if it is associated with a *filter bank*

$$\boldsymbol{\eta} := \{a, b_1, \ldots, b_r\} \subset \ell_2(\mathbb{Z}) \tag{III.2}$$

satisfying

$$\widehat{\alpha}(2\xi) = \widehat{\alpha}(\xi)\widehat{a}(\xi), \quad \widehat{\beta^n}(2\xi) = \widehat{\alpha}(\xi)\widehat{b_n}(\xi), \quad n = 1, \ldots, r. \tag{III.3}$$

Definition III.1. *For a set of scaling functions $\digamma$ given by (III.1), the ($\mathbb{C}^{3\times 3}$-valued) continuous tensor needlets for vector fields on $\mathbb{S}^2$ are*

$$\begin{aligned}
\boldsymbol{\Phi}_{j,\boldsymbol{y}}(\boldsymbol{x}) &:= \sum_{\ell=1}^{\infty} \widehat{\alpha}\left(\frac{\ell}{2^j}\right) \sum_{m=-\ell}^{\ell} \Big(\mathbf{y}_{\ell,m}(\boldsymbol{x}) \otimes \mathbf{y}_{\ell,m}(\boldsymbol{y}) + \mathbf{z}_{\ell,m}(\boldsymbol{x}) \otimes \mathbf{z}_{\ell,m}(\boldsymbol{y})\Big) \\
&= \sum_{\ell=1}^{\infty} \widehat{\alpha}\left(\frac{\ell}{2^j}\right) \Big(\mathbf{p}_\ell(\boldsymbol{x},\boldsymbol{y}) + \mathbf{q}_\ell(\boldsymbol{x},\boldsymbol{y})\Big), \\
\boldsymbol{\Psi}^n_{j,\boldsymbol{y}}(\boldsymbol{x}) &:= \sum_{\ell=1}^{\infty} \widehat{\beta^n}\left(\frac{\ell}{2^j}\right) \sum_{m=-\ell}^{\ell} \Big(\mathbf{y}_{\ell,m}(\boldsymbol{x}) \otimes \mathbf{y}_{\ell,m}(\boldsymbol{y}) + \mathbf{z}_{\ell,m}(\boldsymbol{x}) \otimes \mathbf{z}_{\ell,m}(\boldsymbol{y})\Big) \\
&= \sum_{\ell=1}^{\infty} \widehat{\beta^n}\left(\frac{\ell}{2^j}\right) \Big(\mathbf{p}_\ell(\boldsymbol{x},\boldsymbol{y}) + \mathbf{q}_\ell(\boldsymbol{x},\boldsymbol{y})\Big), \quad n = 1, \ldots, r.
\end{aligned}$$

For $J = 0, 1, \ldots$, the set of tensor needlets

$$\mathsf{CFS}_J := \{\boldsymbol{\Phi}_{J,\boldsymbol{y}}; \boldsymbol{\Psi}^1_{j,\boldsymbol{y}}, \ldots, \boldsymbol{\Psi}^r_{j,\boldsymbol{y}} : j \geq J, \boldsymbol{y} \in \mathbb{S}^2\} \tag{III.4}$$

is called the *continuous needlet system* starting from scale level J with the filter bank $\boldsymbol{\eta}$.

Each continuous needlet is a tensor field on $\mathbb{S}^2$.

We call the continuous tensor needlet system CFS_J a tight needlet system for $\mathbf{L}_2(\mathbb{S}^2)$ if $\mathsf{CFS}_J \subset \mathbf{L}_2(\mathbb{S}^2)$ and if for any $\boldsymbol{f} \in \mathbf{L}_2(\mathbb{S}^2)$,

$$\boldsymbol{f} = \int_{\mathbb{S}^2} \boldsymbol{\Phi}_{J,\boldsymbol{y}} \left\langle \boldsymbol{f}, \boldsymbol{\Phi}_{J,\boldsymbol{y}} \right\rangle^T \mathrm{d}\sigma(\boldsymbol{y}) + \sum_{j=J}^{\infty} \sum_{n=1}^{r} \int_{\mathbb{S}^2} \boldsymbol{\Psi}^n_{j,\boldsymbol{y}} \left\langle \boldsymbol{f}, \boldsymbol{\Psi}^n_{j,\boldsymbol{y}} \right\rangle^T \mathrm{d}\sigma(\boldsymbol{y}), \tag{III.5}$$

in L_2 sense or equivalently,

$$\|\boldsymbol{f}\|^2_{\mathbf{L}_2(\mathbb{S}^2)} = \int_{\mathbb{S}^2} \left|\langle \boldsymbol{f}, \boldsymbol{\Phi}_{J,\boldsymbol{y}}\rangle\right|^2 \, \mathrm{d}\sigma(\boldsymbol{y}) + \sum_{j=J}^{\infty}\sum_{n=1}^{r} \int_{\mathbb{S}^2} \left|\left\langle \boldsymbol{f}, \boldsymbol{\Psi}^n_{j,\boldsymbol{y}}\right\rangle\right|^2 \, \mathrm{d}\sigma(\boldsymbol{y}).$$

The elements of the tight continuous tensor needlet system CFS_J will be called *continuous tight tensor needlets* for $\mathbf{L}_2(\mathbb{S}^2)$.

Theorem III.2. *Let $J_0 \in \mathbb{Z}$ be an integer, $\mathsf{CFS}_J(\boldsymbol{\eta})$, $J \geq J_0$, given in (III.4), be a sequence of continuous tensor needlet systems whose continuous tensor needlets are given by Definition III.1 with filter bank $\boldsymbol{\eta}$ given by (III.2) and scaling functions satisfying (III.3). Then the following statements are equivalent.*
(i) The continuous needlet systems $\mathsf{CFS}_J(\boldsymbol{\eta})$ are tight frames for $\mathbf{L}_2(\mathbb{S}^2)$ for $J \geq J_0$, i.e. (III.5) holds for all $J \geq J_0$.
(ii) For each $\boldsymbol{f} \in \mathbf{L}_2(\mathbb{S}^2)$, the following identities hold.

$$\lim_{j\to\infty} \left\| \int_{\mathbb{S}^2} \boldsymbol{\Phi}_{j,\boldsymbol{y}} \left\langle \boldsymbol{f}, \boldsymbol{\Phi}_{j,\boldsymbol{y}}\right\rangle^T \, \mathrm{d}\sigma(\boldsymbol{y}) - \boldsymbol{f}\right\|_{\mathbf{L}_2(\mathbb{S}^2)} = 0, \tag{III.6}$$

and for all $j \geq J_0$,

$$\int_{\mathbb{S}^2} \boldsymbol{\Phi}_{j+1,\boldsymbol{y}} \left\langle \boldsymbol{f}, \boldsymbol{\Phi}_{j+1,\boldsymbol{y}}\right\rangle^T \, \mathrm{d}\sigma(\boldsymbol{y}) = \int_{\mathbb{S}^2} \boldsymbol{\Phi}_{j,\boldsymbol{y}} \left\langle \boldsymbol{f}, \boldsymbol{\Phi}_{j,\boldsymbol{y}}\right\rangle^T \, \mathrm{d}\sigma(\boldsymbol{y}) + \sum_{n=1}^{r} \int_{\mathbb{S}^2} \boldsymbol{\Psi}^n_{j,\boldsymbol{y}} \left\langle \boldsymbol{f}, \boldsymbol{\Psi}^n_{j,\boldsymbol{y}}\right\rangle^T \, \mathrm{d}\sigma(\boldsymbol{y}). \tag{III.7}$$

(iii) For each $\boldsymbol{f} \in \mathbf{L}_2(\mathbb{S}^2)$, the following identities hold.

$$\lim_{j\to\infty} \int_{\mathbb{S}^2} \left|\langle \boldsymbol{f}, \boldsymbol{\Phi}_{j,\boldsymbol{y}}\rangle\right|^2 \, \mathrm{d}\sigma(\boldsymbol{y}) = \|\boldsymbol{f}\|^2_{\mathbf{L}_2(\mathbb{S}^2)},$$

and for all $j \geq J_0$,

$$\int_{\mathbb{S}^2} \left|\langle \boldsymbol{f}, \boldsymbol{\Phi}_{j+1,\boldsymbol{y}}\rangle\right|^2 \, \mathrm{d}\sigma(\boldsymbol{y}) = \int_{\mathbb{S}^2} \left|\langle \boldsymbol{f}, \boldsymbol{\Phi}_{j,\boldsymbol{y}}\rangle\right|^2 \, \mathrm{d}\sigma(\boldsymbol{y}) + \sum_{n=1}^{r} \int_{\mathbb{S}^2} \left|\left\langle \boldsymbol{f}, \boldsymbol{\Psi}^n_{j,\boldsymbol{y}}\right\rangle\right|^2 \, \mathrm{d}\sigma(\boldsymbol{y}).$$

(iv) The scaling functions in F satisfy

$$\lim_{j\to\infty} \left|\widehat{\alpha}\left(\frac{\lambda_\ell}{2^j}\right)\right| = 1, \quad \ell \geq 1, \tag{III.8}$$

$$\left|\widehat{\alpha}\left(\frac{\lambda_\ell}{2^{j+1}}\right)\right|^2 = \left|\widehat{\alpha}\left(\frac{\lambda_\ell}{2^j}\right)\right|^2 + \sum_{n=1}^{r} \left|\widehat{\beta^n}\left(\frac{\lambda_\ell}{2^j}\right)\right|^2, \quad \ell \geq \ell, \ j \geq J_0. \tag{III.9}$$

(v) The refinable function α satisfies (III.8) and for all ℓ satisfying $\widehat{a}\left(\frac{\lambda_\ell}{2^j}\right) \neq 0$ and $j \geq J_0 + 1$ the filters in the filter bank $\boldsymbol{\eta}$ satisfy

$$\left|\widehat{a}\left(\frac{\lambda_\ell}{2^j}\right)\right|^2 + \sum_{n=1}^{r} \left|\widehat{b_n}\left(\frac{\lambda_\ell}{2^j}\right)\right|^2 = 1.$$

Proof. We first show that "(i) $\Longleftrightarrow$ (ii)". For $j \in \mathbb{N}$, let

$$\mathrm{P}^{(\alpha)}_j \boldsymbol{f} := \int_{\mathbb{S}^2} \boldsymbol{\Phi}_{j,\boldsymbol{y}} \left\langle \boldsymbol{f}, \boldsymbol{\Phi}_{j,\boldsymbol{y}}\right\rangle^T \, \mathrm{d}\sigma(\boldsymbol{y}), \quad \mathrm{P}^{(\beta^n)}_j \boldsymbol{f} := \int_{\mathbb{S}^2} \boldsymbol{\Psi}^n_{j,\boldsymbol{y}} \left\langle \boldsymbol{f}, \boldsymbol{\Psi}^n_{j,\boldsymbol{y}}\right\rangle^T \, \mathrm{d}\sigma(\boldsymbol{y}), \quad \boldsymbol{f} \in \mathbf{L}_2(\mathbb{S}^2).$$

"(i) $\Longleftarrow$ (ii)". If $\mathsf{CFS}_J(\boldsymbol{\eta})$ is a tight frame, then for all $\boldsymbol{f} \in \mathbf{L}_2(\mathbb{S}^2)$ and all $J \geq J_0$

$$\boldsymbol{f} = \mathrm{P}^{(\alpha)}_J \boldsymbol{f} + \sum_{j=J}^{\infty}\sum_{n=1}^{r} \mathrm{P}^{(\beta^n)}_j \boldsymbol{f} = \mathrm{P}^{(\alpha)}_{J+1} \boldsymbol{f} + \sum_{j=J+1}^{\infty}\sum_{n=1}^{r} \mathrm{P}^{(\beta^n)}_j \boldsymbol{f}$$

in L_2 sense. Thus, for $J \geq J_0$,

$$\mathrm{P}_{J+1}^{(\alpha)} \boldsymbol{f} = \mathrm{P}_J^{(\alpha)} \boldsymbol{f} + \sum_{n=1}^{r} \mathrm{P}_J^{(\beta^n)} \boldsymbol{f}. \tag{III.10}$$

This gives (III.7). Recursively using (III.10) we obtain

$$\mathrm{P}_{m+1}^{(\alpha)} \boldsymbol{f} = \mathrm{P}_J^{(\alpha)} \boldsymbol{f} + \sum_{j=J}^{m} \sum_{n=1}^{r} \mathrm{P}_j^{(\beta^n)} \boldsymbol{f} \tag{III.11}$$

for all $m \geq J$ and $J \geq J_0$. If $m \to \infty$ in (III.11), we then obtain

$$\lim_{m\to\infty} \mathrm{P}_{m+1}^{(\alpha)} \boldsymbol{f} = \mathrm{P}_J^{(\alpha)} \boldsymbol{f} + \sum_{j=J}^{\infty} \sum_{n=1}^{r} \mathrm{P}_j^{(\beta^n)} \boldsymbol{f} = \boldsymbol{f}, \quad \boldsymbol{f} \in \mathbf{L}_2(\mathbb{S}^2).$$

This gives (III.6).

"(i)$\Longrightarrow$(ii)". Using (III.7) recursively, we obtain (III.11). If m tends to infinity, with the convergence of (III.6), we obtain the tightness of CFS_J for $J \geq J_0$.

We now prove "(ii)$\Longleftrightarrow$(iv)". By Definition III.1, for $n = 1, \ldots, r$, $j = 0, 1, \ldots$ and $\boldsymbol{y} \in \mathbb{S}^2$,

$$\left\langle \boldsymbol{f}, \boldsymbol{\Phi}_{j,\boldsymbol{y}} \right\rangle^T = \sum_{\ell=0}^{\infty} \overline{\widehat{\alpha}\left(\frac{\lambda_\ell}{2^j}\right)} \sum_{m=-\ell}^{\ell} \left(\widehat{\boldsymbol{f}}_{\ell m} \mathbf{y}_{\ell,m}(\boldsymbol{y}) + \widetilde{\boldsymbol{f}}_{\ell m} \mathbf{z}_{\ell,m}(\boldsymbol{y}) \right)$$

$$\left\langle \boldsymbol{f}, \boldsymbol{\Psi}_{j,\boldsymbol{y}}^n \right\rangle^T = \sum_{\ell=0}^{\infty} \overline{\widehat{\beta^n}\left(\frac{\lambda_\ell}{2^j}\right)} \sum_{m=-\ell}^{\ell} \left(\widehat{\boldsymbol{f}}_{\ell m} \mathbf{y}_{\ell,m}(\boldsymbol{y}) + \widetilde{\boldsymbol{f}}_{\ell m} \mathbf{z}_{\ell,m}(\boldsymbol{y}) \right).$$

Then,

$$\begin{aligned}
\mathrm{P}_j^{(\alpha)} \boldsymbol{f} &= \int_{\mathbb{S}^2} \sum_{\ell=1}^{\infty} \widehat{\alpha}\left(\frac{\lambda_\ell}{2^j}\right) \sum_{m=-\ell}^{\ell} \left(\mathbf{y}_{\ell,m} \otimes \mathbf{y}_{\ell,m}(\boldsymbol{y}) + \mathbf{z}_{\ell,m} \otimes \mathbf{z}_{\ell,m}(\boldsymbol{y}) \right) \\
&\qquad \times \sum_{\ell=1}^{\infty} \overline{\widehat{\alpha}\left(\frac{\lambda_\ell}{2^j}\right)} \sum_{m=-\ell}^{\ell} \left(\widehat{\boldsymbol{f}}_{\ell m} \mathbf{y}_{\ell,m}(\boldsymbol{y}) + \widetilde{\boldsymbol{f}}_{\ell m} \mathbf{z}_{\ell,m}(\boldsymbol{y}) \right) \mathrm{d}\sigma(\boldsymbol{y}) \\
&= \sum_{\ell=1}^{\infty} \sum_{\ell'=1}^{\infty} \overline{\widehat{\alpha}\left(\frac{\lambda_\ell}{2^j}\right)} \widehat{\alpha}\left(\frac{\lambda_{\ell'}}{2^j}\right) \sum_{m=-\ell}^{\ell} \sum_{m'=-\ell'}^{\ell'} \Big(\mathbf{y}_{\ell,m} \left\langle \mathbf{y}_{\ell' m'}, \mathbf{y}_{\ell,m} \right\rangle \widehat{\boldsymbol{f}}_{\ell' m'} + \mathbf{y}_{\ell,m} \left\langle \mathbf{z}_{\ell' m'}, \mathbf{y}_{\ell,m} \right\rangle \widetilde{\boldsymbol{f}}_{\ell' m'} \\
&\qquad + \mathbf{z}_{\ell,m} \left\langle \mathbf{y}_{\ell' m'}, \mathbf{z}_{\ell,m} \right\rangle \widehat{\boldsymbol{f}}_{\ell' m'} + \mathbf{z}_{\ell,m} \left\langle \mathbf{z}_{\ell' m'}, \mathbf{z}_{\ell,m} \right\rangle \widetilde{\boldsymbol{f}}_{\ell' m'} \Big) \\
&= \sum_{\ell=1}^{\infty} \left| \widehat{\alpha}\left(\frac{\lambda_\ell}{2^j}\right) \right|^2 \sum_{m=-\ell}^{\ell} \left(\widehat{\boldsymbol{f}}_{\ell m} \mathbf{y}_{\ell,m} + \widetilde{\boldsymbol{f}}_{\ell m} \mathbf{z}_{\ell,m} \right).
\end{aligned} \tag{III.12}$$

Similarly,

$$\mathrm{P}_j^{(\beta^n)} \boldsymbol{f} = \sum_{\ell=1}^{\infty} \left| \widehat{\beta^n}\left(\frac{\lambda_\ell}{2^j}\right) \right|^2 \sum_{m=-\ell}^{\ell} \left(\widehat{\boldsymbol{f}}_{\ell m} \mathbf{y}_{\ell,m} + \widetilde{\boldsymbol{f}}_{\ell m} \mathbf{z}_{\ell,m} \right).$$

Thus,

$$\widehat{\left(\mathrm{P}_j^{(\alpha)} \boldsymbol{f}\right)}_{\ell m} = \left| \widehat{\alpha}\left(\frac{\lambda_\ell}{2^j}\right) \right|^2 \widehat{\boldsymbol{f}}_{\ell m}, \quad \widetilde{\left(\mathrm{P}_j^{(\alpha)} \boldsymbol{f}\right)}_{\ell m} = \left| \widehat{\alpha}\left(\frac{\lambda_\ell}{2^j}\right) \right|^2 \widetilde{\boldsymbol{f}}_{\ell m}, \tag{III.13}$$

$$\widehat{\left(\mathrm{P}_j^{(\beta^n)} \boldsymbol{f}\right)}_{\ell m} = \left| \widehat{\beta^n}\left(\frac{\lambda_\ell}{2^j}\right) \right|^2 \widehat{\boldsymbol{f}}_{\ell m}, \quad \widetilde{\left(\mathrm{P}_j^{(\beta^n)} \boldsymbol{f}\right)}_{\ell m} = \left| \widehat{\beta^n}\left(\frac{\lambda_\ell}{2^j}\right) \right|^2 \widetilde{\boldsymbol{f}}_{\ell m}. \tag{III.14}$$

This means that (III.7) is equivalent to (III.9). Also, (III.13) and (III.14) give

$$\left\|\mathrm{P}_j^{(\alpha)}\boldsymbol{f}-\boldsymbol{f}\right\|_{\mathbf{L}_2(\mathbb{S}^2)}^2=\sum_{\ell=0}^{\infty}\left(\left|\widehat{\alpha}\left(\frac{\lambda_\ell}{2^j}\right)\right|^2-1\right)^2\sum_{m=-\ell}^{\ell}\left(\left|\widehat{\boldsymbol{f}}_{\ell m}\right|^2+\left|\widetilde{\boldsymbol{f}}_{\ell m}\right|^2\right)$$

and we obtain that (III.6) is equivalent to (III.8).

The equivalence between (iii) and (iv) is well-known, see e.g. [23]. The equivalence between (iv) and (v) follows from (III.3). □

A *quadrature rule* on $\mathbb{S}^2$ is a set of N pairs of weights and points on $\mathbb{S}^2$

$$\mathcal{Q}_N=\{(\omega_i,\boldsymbol{x}_i):\omega_i\in\mathbb{R},\boldsymbol{x}_i\in\mathbb{S}^2,i=1,\dots,N\}.$$

For $L\geq 0$, let $\Pi_L:=\operatorname{span}\{Y_{\ell,m}:\ell=0,\dots,L,\ m=-\ell,\dots,\ell\}$ be a polynomial space of degree L. Elements of Π_L are called polynomials of degree L. The quadrature rule $\mathcal{Q}_N$ is called exact for polynomials of degree L if for any $P\in\Pi_L$

$$\int_{\mathbb{S}^2}P(\boldsymbol{x})\,\mathrm{d}\sigma(\boldsymbol{x})=\sum_{i=1}^{N}\omega_iP(\boldsymbol{x}_i).$$

To obtain semi-discrete needlets, we discretize the integrals in (III.5) by quadrature rules for different scales.

Definition III.3. *Let a set of scaling functions F be given by (III.1) and a sequence of quadrature rules $\mathcal{Q}_{N_j}=\{(\omega_{j,k},\boldsymbol{x}_{j,k})\}_{k=1}^{N_j}$ be exact for polynomials of degree 2^{2j}. Then, for $j=0,1,\dots,$ and $k=1,\dots,N_j$, the ($\mathbb{C}^{d\times d}$-valued semi-discrete) tensor needlets for vector fields on $\mathbb{S}^2$ are given by*

$$\begin{aligned}\boldsymbol{\Phi}_{j,k}(\boldsymbol{x})&:=\sqrt{\omega_{j,k}}\,\boldsymbol{\Phi}_{j,\boldsymbol{x}_{j,k}}(\boldsymbol{x})\\&=\sqrt{\omega_{j,k}}\sum_{\ell=1}^{\infty}\widehat{\alpha}\left(\frac{\lambda_\ell}{2^j}\right)\sum_{m=-\ell}^{\ell}\left(\mathbf{y}_{\ell,m}(\boldsymbol{x})\otimes\mathbf{y}_{\ell,m}(\boldsymbol{x}_{j,k})+\mathbf{z}_{\ell,m}(\boldsymbol{x})\otimes\mathbf{z}_{\ell,m}(\boldsymbol{x}_{j,k})\right)\\&=\sqrt{\omega_{j,k}}\sum_{\ell=1}^{\infty}\widehat{\alpha}\left(\frac{\lambda_\ell}{2^j}\right)\left(\mathbf{p}_\ell(\boldsymbol{x},\boldsymbol{x}_{j,k})+\mathbf{q}_\ell(\boldsymbol{x},\boldsymbol{x}_{j,k})\right),\end{aligned}$$

and for $n=1,\dots,r$, $j=0,1,\dots,$ and $k'=1,\dots,N_{j+1}$,

$$\begin{aligned}\boldsymbol{\Psi}_{j,k'}^n(\boldsymbol{x})&:=\sqrt{\omega_{j+1,k'}}\,\boldsymbol{\Psi}_{j,\boldsymbol{x}_{j+1,k'}}^n(\boldsymbol{x})\\&=\sqrt{\omega_{j+1,k'}}\sum_{\ell=1}^{\infty}\widehat{\beta^n}\left(\frac{\lambda_\ell}{2^j}\right)\sum_{m=-\ell}^{\ell}\left(\mathbf{y}_{\ell,m}(\boldsymbol{x})\otimes\mathbf{y}_{\ell,m}(\boldsymbol{x}_{j+1,k'})+\mathbf{z}_{\ell,m}(\boldsymbol{x})\otimes\mathbf{z}_{\ell,m}(\boldsymbol{x}_{j+1,k'})\right)\\&=\sqrt{\omega_{j+1,k'}}\sum_{\ell=1}^{\infty}\widehat{\beta^n}\left(\frac{\lambda_\ell}{2^j}\right)\left(\mathbf{p}_\ell(\boldsymbol{x},\boldsymbol{x}_{j+1,k'})+\mathbf{q}_\ell(\boldsymbol{x},\boldsymbol{x}_{j+1,k'})\right).\end{aligned}$$

For $J=0,1,\dots,$ the set of needlets

$$\mathsf{FS}_J:=\mathsf{FS}_J(\boldsymbol{\eta};\{\mathcal{Q}_{N_j}\}_{j\geq J}):=\{\boldsymbol{\Phi}_{J,k};\boldsymbol{\Psi}_{j,k'}^1,\dots,\boldsymbol{\Psi}_{j,k'}^r:j\geq J,\ k=1,\dots,N_J,\ k'=1,\dots,N_{j+1}\}\quad\text{(III.15)}$$

is called the *(semi-discrete) tensor needlet system* starting from the scale level J with the filter bank $\boldsymbol{\eta}$.

The tensor needlet system FS_J is called a tight needlet system for $L_2(\mathbb{S}^2)$ if $\mathsf{FS}_J \subset L_2(\mathbb{S}^2)$ and for any $\boldsymbol{f} \in \mathbf{L}_2(\mathbb{S}^2)$

$$\boldsymbol{f} = \sum_{k=1}^{N_J} \boldsymbol{\Phi}_{J,k} \left\langle \boldsymbol{f}, \boldsymbol{\Phi}_{J,k} \right\rangle^T + \sum_{j=J}^{\infty} \sum_{k=1}^{N_{j+1}} \sum_{n=1}^{r} \boldsymbol{\Psi}_{j,k}^n \left\langle \boldsymbol{f}, \boldsymbol{\Psi}_{j,k}^n \right\rangle^T \tag{III.16}$$

in L_2 sense or equivalently,

$$\|\boldsymbol{f}\|_{\mathbf{L}_2(\mathbb{S}^2)}^2 = \sum_{k=1}^{N_J} \left| \langle \boldsymbol{f}, \boldsymbol{\Phi}_{J,k} \rangle \right|^2 + \sum_{j=J}^{\infty} \sum_{k=1}^{N_{j+1}} \sum_{n=1}^{r} \left| \left\langle \boldsymbol{f}, \boldsymbol{\Psi}_{j,k}^n \right\rangle \right|^2.$$

The elements of the tight tensor needlet system FS_J are said to be *(semi-discrete) tight tensor needlets* for $\mathbf{L}_2(\mathbb{S}^2)$.

Theorem III.4. *Let $\mathsf{FS}_J(\boldsymbol{\eta}; \{\mathcal{Q}_{N_j}\}_{j \geq J})$, $J \geq J_0$, given in (III.15) be a sequence of tensor needlet systems with elements given by Definition III.1 and the filter bank $\boldsymbol{\eta}$ given by (III.2), scaling functions satisfying (III.3). Let a sequence of quadrature rules $\mathcal{Q}_{N_j} = \{(\omega_{j,k}, \boldsymbol{x}_{j,k})\}_{k=1}^{N_j}$ be exact for degree 2^{j+1}, $j = 0, 1, \ldots$. Then, the following statements are equivalent.*

(i) The continuous needlet systems FS_J are tight frames for $\mathbf{L}_2(\mathbb{S}^2)$ for $J \geq J_0$, i.e. (III.16) holds for all $J \geq J_0$.

(ii) For each $\boldsymbol{f} \in \mathbf{L}_2(\mathbb{S}^2)$, the following identities hold.

$$\lim_{j \to \infty} \left\| \sum_{k=1}^{N_j} \boldsymbol{\Phi}_{j,k} \left\langle \boldsymbol{f}, \boldsymbol{\Phi}_{j,k} \right\rangle^T - \boldsymbol{f} \right\|_{\mathbf{L}_2(\mathbb{S}^2)} = 0$$

and for $j \geq J_0$

$$\sum_{k=1}^{N_{j+1}} \boldsymbol{\Phi}_{j+1,k} \left\langle \boldsymbol{f}, \boldsymbol{\Phi}_{j+1,k} \right\rangle^T = \sum_{k=1}^{N_j} \boldsymbol{\Phi}_{j,k} \left\langle \boldsymbol{f}, \boldsymbol{\Phi}_{j,k} \right\rangle^T + \sum_{k=1}^{N_{j+1}} \sum_{n=1}^{r} \boldsymbol{\Psi}_{j,k}^n \left\langle \boldsymbol{f}, \boldsymbol{\Psi}_{j,k}^n \right\rangle^T.$$

(iii) For each $\boldsymbol{f} \in \mathbf{L}_2(\mathbb{S}^2)$, the following identities hold.

$$\lim_{j \to \infty} \sum_{k=1}^{N_j} \left| \langle \boldsymbol{f}, \boldsymbol{\Phi}_{j,k} \rangle \right|^2 = \|\boldsymbol{f}\|_{\mathbf{L}_2(\mathbb{S}^2)}^2$$

and for $j \geq J_0$

$$\sum_{k=1}^{N_{j+1}} \left| \langle \boldsymbol{f}, \boldsymbol{\Phi}_{j+1,k} \rangle \right|^2 = \sum_{k=1}^{N_j} \left| \langle \boldsymbol{f}, \boldsymbol{\Phi}_{j,k} \rangle \right|^2 + \sum_{k=1}^{N_{j+1}} \sum_{n=1}^{r} \left| \left\langle \boldsymbol{f}, \boldsymbol{\Psi}_{j,k}^n \right\rangle \right|^2.$$

(iv) The scaling functions in $\digamma$ satisfy

$$\lim_{j \to \infty} \left| \widehat{\alpha} \left(\frac{\lambda_\ell}{2^j} \right) \right| = 1, \quad \ell \geq 1, \tag{III.17}$$

$$\left| \widehat{\alpha} \left(\frac{\lambda_\ell}{2^{j+1}} \right) \right|^2 = \left| \widehat{\alpha} \left(\frac{\lambda_\ell}{2^j} \right) \right|^2 + \sum_{n=1}^{r} \left| \widehat{\beta^n} \left(\frac{\lambda_\ell}{2^j} \right) \right|^2, \quad \ell \geq \ell, \ j \geq J_0.$$

(v) The refinable function α satisfies (III.17) and for all ℓ satisfying $\widehat{a}\left(\frac{\lambda_\ell}{2^j}\right) \neq 0$ and $j \geq J_0 + 1$ the filters in the filter bank $\boldsymbol{\eta}$ satisfy

$$\left| \widehat{a} \left(\frac{\lambda_\ell}{2^j} \right) \right|^2 + \sum_{n=1}^{r} \left| \widehat{b_n} \left(\frac{\lambda_\ell}{2^j} \right) \right|^2 = 1. \tag{III.18}$$

Proof. Since the components of $\mathbf{y}_{\ell,m}$ and $\mathbf{z}_{\ell,m}$ are scalar polynomials on $\mathbb{S}^2$ with degrees not exceeding ℓ, $\overline{\mathbf{y}_{\ell,m}(\boldsymbol{x})}^T\mathbf{y}_{\ell'm'}(\boldsymbol{x})$, $\overline{\mathbf{y}_{\ell,m}(\boldsymbol{x})}^T\mathbf{z}_{\ell'm'}(\boldsymbol{x})$, $\overline{\mathbf{z}_{\ell,m}(\boldsymbol{x})}\mathbf{z}_{\ell'm'}(\boldsymbol{x})$ and their complex conjugates are scalar polynomials of $\boldsymbol{x}$ with degrees not exceeding $\ell+\ell'$. For $j\geq 0$, as $\{(\omega_{j,k},\boldsymbol{x}_{j,k})\}_{k=1}^{N_j}$ is a quadrature rule exact for degree 2^{j+1}, by the orthogonality of $\mathbf{y}_{\ell,m}$ and $\mathbf{z}_{\ell,m}$, for $\ell,\ell\geq 1$, $m,m'=-\ell,\ldots,\ell$, one gets

$$\sum_{k=1}^{N_j}\omega_{j,k}\,\overline{\mathbf{y}_{\ell,m}(\boldsymbol{x}_{j,k})}^T\mathbf{y}_{\ell'm'}(\boldsymbol{x}_{j,k})=\sum_{k=1}^{N_j}\omega_{j,k}\,\overline{\mathbf{z}_{\ell,m}(\boldsymbol{x}_{j,k})}^T\mathbf{z}_{\ell'm'}(\boldsymbol{x}_{j,k})=\delta_{\ell\ell'}\delta_{mm'},\tag{III.19}$$

$$\sum_{k=1}^{N_j}\omega_{j,k}\,\overline{\mathbf{y}_{\ell,m}(\boldsymbol{x}_{j,k})}^T\mathbf{z}_{\ell'm'}(\boldsymbol{x}_{j,k})=\sum_{k=1}^{N_j}\omega_{j,k}\,\overline{\mathbf{z}_{\ell,m}(\boldsymbol{x}_{j,k})}^T\mathbf{y}_{\ell'm'}(\boldsymbol{x}_{j,k})=0.\tag{III.20}$$

By Definition III.3, for $n=1,\ldots,r$ and $k=1,\ldots,N_j$, $j=0,1,\ldots$, it follows

$$\langle\boldsymbol{f},\boldsymbol{\Phi}_{j,k}\rangle^T=\sum_{\ell=1}^{\infty}\sqrt{\omega_{j,k}}\,\overline{\widehat{\alpha}\left(\frac{\lambda_\ell}{2^j}\right)}\sum_{m=-\ell}^{\ell}\left(\widehat{\boldsymbol{f}}_{\ell m}\mathbf{y}_{\ell,m}(\boldsymbol{x}_{j,k})+\widetilde{\boldsymbol{f}}_{\ell m}\mathbf{z}_{\ell,m}(\boldsymbol{x}_{j,k})\right)\tag{III.21}$$

$$\left\langle\boldsymbol{f},\boldsymbol{\Psi}_{j,k}^n\right\rangle^T=\sum_{\ell=1}^{\infty}\sqrt{\omega_{j+1,k}}\,\overline{\widehat{\beta^n}\left(\frac{\lambda_\ell}{2^j}\right)}\sum_{m=-\ell}^{\ell}\left(\widehat{\boldsymbol{f}}_{\ell m}\mathbf{y}_{\ell,m}(\boldsymbol{x}_{j,k})+\widetilde{\boldsymbol{f}}_{\ell m}\mathbf{z}_{\ell,m}(\boldsymbol{x}_{j,k})\right).\tag{III.22}$$

Then,

$$\begin{aligned}
&\sum_{k=1}^{N_j}\boldsymbol{\Phi}_{j,k}\langle\boldsymbol{f},\boldsymbol{\Phi}_{j,k}\rangle^T\\
&=\sum_{k=1}^{N_j}\sum_{\ell=1}^{\infty}\omega_{j,k}\,\widehat{\alpha}\left(\frac{\lambda_\ell}{2^j}\right)\sum_{m=-\ell}^{\ell}\left(\mathbf{y}_{\ell,m}\otimes\mathbf{y}_{\ell,m}(\boldsymbol{x}_{j,k})+\mathbf{z}_{\ell,m}\otimes\mathbf{z}_{\ell,m}(\boldsymbol{x}_{j,k})\right)\\
&\qquad\times\sum_{\ell=1}^{\infty}\overline{\widehat{\alpha}\left(\frac{\lambda_\ell}{2^j}\right)}\sum_{m=-\ell}^{\ell}\left(\widehat{\boldsymbol{f}}_{\ell m}\mathbf{y}_{\ell,m}(\boldsymbol{x}_{j,k})+\widetilde{\boldsymbol{f}}_{\ell m}\mathbf{z}_{\ell,m}(\boldsymbol{x}_{j,k})\right)\\
&=\sum_{k=1}^{N_j}\sum_{\ell=1}^{\infty}\sum_{\ell'=1}^{\infty}\omega_{j,k}\,\widehat{\alpha}\left(\frac{\lambda_\ell}{2^j}\right)\overline{\widehat{\alpha}\left(\frac{\lambda_{\ell'}}{2^j}\right)}\sum_{m=-\ell}^{\ell}\sum_{m'=-\ell'}^{\ell'}\left(\mathbf{y}_{\ell,m}\overline{\mathbf{y}_{\ell,m}(\boldsymbol{x}_{j,k})}^T+\mathbf{z}_{\ell,m}\overline{\mathbf{z}_{\ell,m}(\boldsymbol{x}_{j,k})}^T\right)\\
&\qquad\times\left(\widehat{\boldsymbol{f}}_{\ell'm'}\mathbf{y}_{\ell'm'}(\boldsymbol{x}_{j,k})+\widetilde{\boldsymbol{f}}_{\ell'm'}\mathbf{z}_{\ell'm'}(\boldsymbol{x}_{j,k})\right)\\
&=\sum_{\ell=1}^{\infty}\sum_{\ell'=1}^{\infty}\widehat{\alpha}\left(\frac{\lambda_\ell}{2^j}\right)\overline{\widehat{\alpha}\left(\frac{\lambda_{\ell'}}{2^j}\right)}\sum_{m=-\ell}^{\ell}\sum_{m'=-\ell'}^{\ell'}\left(\mathbf{y}_{\ell,m}\sum_{k=1}^{N_j}\omega_{j,k}\,\overline{\mathbf{y}_{\ell,m}(\boldsymbol{x}_{j,k})}^T\mathbf{y}_{\ell'm'}(\boldsymbol{x}_{j,k})\widehat{\boldsymbol{f}}_{\ell'm'}\right.\\
&\quad+\mathbf{y}_{\ell,m}\sum_{k=1}^{N_j}\omega_{j,k}\,\overline{\mathbf{y}_{\ell,m}(\boldsymbol{x}_{j,k})}^T\mathbf{z}_{\ell'm'}(\boldsymbol{x}_{j,k})\widetilde{\boldsymbol{f}}_{\ell'm'}+\mathbf{z}_{\ell,m}\sum_{k=1}^{N_j}\omega_{j,k}\,\overline{\mathbf{z}_{\ell,m}(\boldsymbol{x}_{j,k})}^T\mathbf{y}_{\ell'm'}(\boldsymbol{x}_{j,k})\widehat{\boldsymbol{f}}_{\ell'm'}\\
&\quad\left.+\mathbf{z}_{\ell,m}\sum_{k=1}^{N_j}\omega_{j,k}\,\overline{\mathbf{z}_{\ell,m}(\boldsymbol{x}_{j,k})}^T\mathbf{z}_{\ell'm'}(\boldsymbol{x}_{j,k})\widetilde{\boldsymbol{f}}_{\ell'm'}\right).
\end{aligned}$$

Then, by (III.19), (III.20) and (III.12), for $j=0,1,\ldots,$

$$\sum_{k=1}^{N_j}\boldsymbol{\Phi}_{j,k}\langle\boldsymbol{f},\boldsymbol{\Phi}_{j,k}\rangle^T=\sum_{\ell=1}^{\infty}\left|\widehat{\alpha}\left(\frac{\lambda_\ell}{2^j}\right)\right|^2\sum_{m=-\ell}^{\ell}\left(\widehat{\boldsymbol{f}}_{\ell m}\mathbf{y}_{\ell,m}+\widetilde{\boldsymbol{f}}_{\ell m}\mathbf{z}_{\ell,m}\right)=\int_{\mathbb{S}^2}\boldsymbol{\Phi}_{j,\boldsymbol{y}}\langle\boldsymbol{f},\boldsymbol{\Phi}_{j,\boldsymbol{y}}\rangle^T\,\mathrm{d}\sigma(\boldsymbol{y}).$$

In a similar way, we obtain that for $n = 1, \ldots, r$ and $j = 0, 1, \ldots,$

$$\sum_{k=1}^{N_j} \mathbf{\Psi}_{j,k}^n \left\langle \boldsymbol{f}, \mathbf{\Psi}_{j,k}^n \right\rangle^T = \sum_{\ell=1}^{\infty} \left| \widehat{\beta^n} \left(\frac{\lambda_\ell}{2^j} \right) \right|^2 \sum_{m=-\ell}^{\ell} \left(\widehat{\boldsymbol{f}}_{\ell m} \mathbf{y}_{\ell,m} + \widetilde{\boldsymbol{f}}_{\ell m} \mathbf{z}_{\ell,m} \right) = \int_{\mathbb{S}^2} \mathbf{\Psi}_{j,\boldsymbol{y}}^n \left\langle \boldsymbol{f}, \mathbf{\Psi}_{j,\boldsymbol{y}}^n \right\rangle^T \mathrm{d}\sigma(\boldsymbol{y}).$$

Thus, (ii) is equivalent to (ii) in Theorem III.2. Then (i), (ii), (iv) and (v) are equivalent. The equivalence between (ii) and (iii) follows from the polarization identity. □

IV. Fast Needlet Transforms

In this section, we discuss the multi-level filter bank transforms associated with a sequence of tight tensor needlets $\mathsf{FS}_J(\boldsymbol{\eta}; \{\mathcal{Q}_{N_j}\}_{j \geq J})$ for $\mathbf{L}_2(\mathbb{S}^2)$. The transforms include the *decomposition* and the *reconstruction*. The decomposition of $\mathrm{v}_j = (\mathrm{v}_{j,k})_{k=1}^{N_j} = (\langle \boldsymbol{f}, \mathbf{\Phi}_{j,k} \rangle^T)_{k=1}^{N_j}$ is into a coarse scale *approximation coefficient sequence* $\mathrm{v}_{j-1} = (\langle \boldsymbol{f}, \mathbf{\Phi}_{j-1,k} \rangle^T)_{k=1}^{N_{j-1}}$ and into the coarse scale *detail coefficient sequences* $\mathrm{w}_{j-1}^n = (\mathrm{w}_{j-1,k}^n)_{k=1}^{N_j} = (\langle \boldsymbol{f}, \mathbf{\Psi}_{j-1,k}^n \rangle^T)_{k=1}^{N_j}$, $n = 1, \ldots, r$. The reconstruction of v_j is an inverse process from the coarse scale approximations and details to fine scales. We show that the decomposition and reconstruction algorithms for the filter bank transforms can be implemented based on discrete Fourier transforms on $\mathbb{S}^2$. In particular, with the employment of fast discrete Fourier transforms (FFTs) for vector spherical harmonics on $\mathbb{S}^2$, we are able to develop fast algorithmic realizations for the multi-level filter bank transforms, that is, fast algorithm for tensor needlet transforms.

A. Multi-level filter bank transforms

The multi-level framelet filter bank transform algorithms that use convolution, downsampling and upsampling for data sequences on $\mathbb{S}^2$, are introduced in this section.

Let $\{\mathcal{Q}_{N_j}\}_{j=J_0}^{\infty}$ be a sequence of quadrature rules on $\mathbb{S}^2$ with $\mathcal{Q}_{N_j} = \{(\omega_{j,k}, \boldsymbol{x}_{j,k}) \in \mathbb{R} \times \mathbb{S}^2 : k = 0, \ldots, N_j\}$ a polynomial-exact quadrature rule of degree 2^j. For an integer $N \in \mathbb{N}_0$, let $l(N)$ be the set of complex-valued sequences on $[0, N]$. Let $\Lambda_j := \dim \Pi_{2^{j-1}} = \#\{\ell \in \mathbb{N}_0 : \lambda_\ell \leq 2^{j-1}\}$. The following transforms (operators or operations) between sequences in $l(\Lambda_j)$ and sequences in $l(N_j)$ are used to describe and implement the algorithms.

Let $h \in l_1(\mathbb{Z})$ be a mask (filter). The *discrete convolution* $\mathrm{v} *_j h$ of a sequence $\mathrm{v} \in l(\Lambda_j, N_j)$ with a mask h is a sequence in $l(\Lambda_j, N_j)$ defined as

$$(\mathrm{v} *_j h)_k := \sum_{\ell=0}^{\Lambda_j} \widehat{h} \left(\frac{\lambda_\ell}{2^j} \right) \sqrt{\omega_{j,k}} \sum_{m=-\ell}^{\ell} \left(\hat{\mathrm{v}}_{\ell,m} \mathbf{y}_{\ell,m}(\boldsymbol{x}_{j,k}) + \tilde{\mathrm{v}}_{\ell,m} \mathbf{z}_{\ell,m}(\boldsymbol{x}_{j,k}) \right), \quad k = 0, \ldots, N_j. \tag{IV.1}$$

The *downsampling operator* $\downarrow_j$: $l(\Lambda_j, N_j) \to l(N_{j-1})$ for a (Λ_j, N_j)-sequence v is

$$(\mathrm{v}\downarrow_j)_k := \sum_{\ell=0}^{\Lambda_j} \sqrt{\omega_{j-1,k}} \sum_{m=-\ell}^{\ell} \left(\hat{\mathrm{v}}_{\ell,m} \mathbf{y}_{\ell,m}(\boldsymbol{x}_{j-1,k}) + \tilde{\mathrm{v}}_{\ell,m} \mathbf{z}_{\ell,m}(\boldsymbol{x}_{j-1,k}) \right), \quad k = 1, \ldots, N_{j-1}. \tag{IV.2}$$

The *upsampling operator* $\uparrow_j$: $l(\Lambda_{j-1}, N_{j-1}) \to l(\Lambda_j, N_j)$ for a (Λ_{j-1}, N_{j-1})-sequence v is

$$(\mathrm{v}\uparrow_j)_k := \sum_{\ell=0}^{\Lambda_{j-1}} \sqrt{\omega_{j,k}} \sum_{m=-\ell}^{\ell} \left(\hat{\mathrm{v}}_{\ell,m} \mathbf{y}_{\ell,m}(\boldsymbol{x}_{j,k}) + \tilde{\mathrm{v}}_{\ell,m} \mathbf{z}_{\ell,m}(\boldsymbol{x}_{j,k}) \right), \quad k = 1, \ldots, N_j. \tag{IV.3}$$

For a mask h, let $h^\star$ be the mask satisfying $\widehat{h^\star}(\xi) = \overline{\widehat{h}(\xi)}$, $\xi \in \mathbb{R}$. The above convolution, downsampling and upsampling give the implementation for decomposition and reconstruction, as follows.

Theorem IV.1. *Let $\mathsf{FS}_J(\boldsymbol{\eta}; \{\mathcal{Q}_{N_j}\}_{j\geq J})$, $J \geq J_0$, given in (III.15) be a sequence of tensor needlet systems whose tensor needlets are given by Definition III.1 with the filter bank $\boldsymbol{\eta}$ given by (III.2), scaling functions in (III.1) and with a sequence of quadrature rules $\mathcal{Q}_{N_j} = \{(\omega_{j,k}, \boldsymbol{x}_{j,k})\}_{k=1}^{N_j}$ which is exact for degree 2^{j+1}, $j = 0, 1, \ldots$. Let $\mathrm{v}_j = (\mathrm{v}_{j,k})_{k=1}^{N_j}$ and $\mathrm{w}_j^n = (\mathrm{w}_{j,k}^n)_{k=1}^{N_{j+1}}$, $n = 1, \ldots, r$, be the approximation coefficient sequence and detail coefficient sequences of $f \in \mathbf{L}_2(\mathbb{S}^2)$ at scale j given by*

$$\mathrm{v}_{j,k} := \langle \boldsymbol{f}, \boldsymbol{\Phi}_{j,k} \rangle^T, \ k = 1, \ldots, N_j, \quad \textit{and} \quad \mathrm{w}_{j,k}^n := \langle \boldsymbol{f}, \boldsymbol{\Psi}_{j,k}^n \rangle^T, \ k = 1, \ldots, N_{j+1}, \ n = 1, \ldots, r, \tag{IV.4}$$

respectively. Then, (i)

1) the coefficient sequence v_j is a (Λ_j, N_j)-seqeunce and $\mathrm{w}_j^n, n = 1, \ldots, r$, are (Λ_{j+1}, N_{j+1})-seqeunces for all $j \geq J_0$;
2) for any $j \geq J_0 + 1$, the following decomposition relations hold:

$$\mathrm{v}_{j-1} = (\mathrm{v}_j *_j a^\star)\downarrow_j, \quad \mathrm{w}_{j-1}^n = \mathrm{v}_j *_j (b_n)^\star, \quad n = 1, \ldots, r; \tag{IV.5}$$

3) for any $j \geq J_0 + 1$, the following reconstruction relation holds:

$$\mathrm{v}_j = (\mathrm{v}_{j-1}\uparrow_j) *_j a + \sum_{n=1}^{r} \mathrm{w}_{j-1}^n *_j b_n. \tag{IV.6}$$

Proof. For v_j and w_{j-1}^n in (IV.4), by (III.21), (III.22), (III.3) and $\operatorname{supp} \widehat{\alpha} \subseteq [0, 1/c]$, we obtain that $\operatorname{supp} \widehat{\beta^n} \subseteq [0, 2/c]$,

$$\mathrm{v}_{j,k} = \sum_{\ell=0}^{\Lambda_j} \overline{\widehat{\alpha}\left(\frac{\lambda_\ell}{2^j}\right)} \sqrt{\omega_{j,k}} \sum_{m=-\ell}^{\ell} \left(\widehat{\boldsymbol{f}}_{\ell m} \mathbf{y}_{\ell,m}(\boldsymbol{x}_{j,k}) + \widetilde{\boldsymbol{f}}_{\ell m} \mathbf{z}_{\ell,m}(\boldsymbol{x}_{j,k}) \right)$$

and

$$\mathrm{w}_{j-1,k}^n = \sum_{\ell=0}^{\Lambda_j} \overline{\widehat{\beta^n}\left(\frac{\lambda_\ell}{2^{j-1}}\right)} \sqrt{\omega_{j,k}} \sum_{m=-\ell}^{\ell} \left(\widehat{\boldsymbol{f}}_{\ell m} \mathbf{y}_{\ell,m}(\boldsymbol{x}_{j,k}) + \widetilde{\boldsymbol{f}}_{\ell m} \mathbf{z}_{\ell,m}(\boldsymbol{x}_{j,k}) \right),$$

where $\widetilde{\boldsymbol{f}}_{\ell m}$ is the curl-free component of $\boldsymbol{f}$. Hence, v_j and w_{j-1}^n, $n = 1, \ldots, r$, are (Λ_j, N_j)-sequences with the discrete Fourier coefficients $\hat{\mathrm{v}}_j := (\hat{\mathrm{v}}_{j,\ell})_{\ell=1}^{\Lambda_j}$, $\hat{\mathrm{w}}_{j-1}^n := (\hat{\mathrm{w}}_{j-1,\ell}^n)_{\ell=1}^{\Lambda_j}$, $\tilde{\mathrm{v}}_j := (\tilde{\mathrm{v}}_{j,\ell})_{\ell=1}^{\Lambda_j}$ and $\tilde{\mathrm{w}}_{j-1}^n := (\tilde{\mathrm{w}}_{j-1,\ell}^n)_{\ell=1}^{\Lambda_j}$ given by

$$\hat{\mathrm{v}}_{j,\ell,m} = \widehat{\boldsymbol{f}}_{\ell m} \overline{\widehat{\alpha}\left(\frac{\lambda_\ell}{2^j}\right)}, \quad \hat{\mathrm{w}}_{j-1,\ell,m}^n = \widehat{\boldsymbol{f}}_{\ell m} \overline{\widehat{\beta^n}\left(\frac{\lambda_\ell}{2^j}\right)}, \quad \ell = 1, \ldots, \Lambda_j,$$

$$\tilde{\mathrm{v}}_{j,\ell,m} = \widetilde{\boldsymbol{f}}_{\ell m} \overline{\widehat{\alpha}\left(\frac{\lambda_\ell}{2^j}\right)}, \quad \tilde{\mathrm{w}}_{j-1,\ell,m}^n = \widetilde{\boldsymbol{f}}_{\ell m} \overline{\widehat{\beta^n}\left(\frac{\lambda_\ell}{2^j}\right)}, \quad \ell = 1, \ldots, \Lambda_j.$$

Thus, statement (i) holds.

Note that v_{j-1} is a (Λ_{j-1}, N_{j-1})-sequence. For $k = 1, \ldots, N_{j-1}$, by (III.3), we can obtain

$$\begin{aligned}
\mathrm{v}_{j-1,k} &= \sum_{\ell=1}^{\Lambda_{j-1}} \overline{\widehat{\alpha}\left(\frac{\lambda_\ell}{2^{j-1}}\right)} \sqrt{\omega_{j-1,k}} \sum_{m=-\ell}^{\ell} \left(\widehat{\boldsymbol{f}}_{\ell m} \mathbf{y}_{\ell,m}(\boldsymbol{x}_{j-1.k}) + \widetilde{\boldsymbol{f}}_{\ell m} \mathbf{z}_{\ell,m}(\boldsymbol{x}_{j-1.k})\right) \\
&= \sum_{\ell=1}^{\Lambda_{j-1}} \overline{\widehat{\alpha}\left(\frac{\lambda_\ell}{2^{j}}\right)} \overline{\widehat{a}\left(\frac{\lambda_\ell}{2^{j}}\right)} \sqrt{\omega_{j-1,k}} \sum_{m=-\ell}^{\ell} \left(\widehat{\boldsymbol{f}}_{\ell m} \mathbf{y}_{\ell,m}(\boldsymbol{x}_{j-1.k}) + \widetilde{\boldsymbol{f}}_{\ell m} \mathbf{z}_{\ell,m}(\boldsymbol{x}_{j-1.k})\right) \\
&= \sum_{\ell=1}^{\Lambda_{j}} \overline{\widehat{a}\left(\frac{\lambda_\ell}{2^{j}}\right)} \sqrt{\omega_{j-1,k}} \sum_{m=-\ell}^{\ell} \left(\hat{\mathrm{v}}_{j,\ell,m} \mathbf{y}_{\ell,m}(\boldsymbol{x}_{j-1.k}) + \tilde{\mathrm{v}}_{j,\ell,m} \mathbf{z}_{\ell,m}(\boldsymbol{x}_{j-1.k})\right) \\
&= \left((\mathrm{v}_j *_j a^\star)\downarrow_j\right)_k.
\end{aligned}$$

Similarly, for $k = 0, \ldots, N_{j-1}$ and $n = 1, \ldots, r$,

$$\begin{aligned}
\mathrm{w}^n_{j-1,k} &= \sum_{\ell=1}^{\Lambda_{j}} \overline{\widehat{\beta^n}\left(\frac{\lambda_\ell}{2^{j-1}}\right)} \sqrt{\omega_{j-1,k}} \sum_{m=-\ell}^{\ell} \left(\hat{\mathrm{w}}^n_{j-1,\ell,m} \mathbf{y}_{\ell,m}(\boldsymbol{x}_{j-1.k}) + \tilde{\mathrm{w}}^n_{j-1,\ell,m} \mathbf{z}_{\ell,m}(\boldsymbol{x}_{j-1.k})\right) \\
&= (\mathrm{v}_j *_j (b_n)^\star)_k.
\end{aligned}$$

This proves (IV.5), thus, statement (ii) holds.

Using $\mathrm{v}_{j-1} = (\mathrm{v}_j *_j a^\star)\downarrow_j$ and $\mathrm{w}^n_{j-1} = \mathrm{v}_j *_j (b_n)^\star$, we obtain

$$\breve{\mathrm{v}} := (\mathrm{v}_{j-1}\uparrow_j) *_j a + \sum_{n=1}^{r} \mathrm{w}^n_{j-1} *_j b_n = (((\mathrm{v}_j *_j a^\star)\downarrow_j)\uparrow_j) *_j a + \sum_{n=1}^{r} (\mathrm{v}_j *_j (b_n)^\star) *_j b_n.$$

This with (IV.1), (IV.2), (IV.3) and (III.18) gives

$$\begin{aligned}
\breve{\mathrm{v}}_k &= \sum_{\ell=0}^{\Lambda_j} \left(\left|\widehat{a}\left(\frac{\lambda_\ell}{2^j}\right)\right|^2 + \sum_{n=1}^{r} \left|\widehat{b_n}\left(\frac{\lambda_\ell}{2^j}\right)\right|^2\right) \sqrt{\omega_{j,k}} \sum_{m=-\ell}^{\ell} \left(\hat{\mathrm{v}}_{j,\ell,m} \mathbf{y}_{\ell,m}(\boldsymbol{x}_{j,k}) + \tilde{\mathrm{v}}_{j,\ell,m} \mathbf{z}_{\ell,m}(\boldsymbol{x}_{j,k})\right) \\
&= \sum_{\ell=0}^{\Lambda_j} \sqrt{\omega_{j,k}} \sum_{m=-\ell}^{\ell} \left(\hat{\mathrm{v}}_{j,\ell,m} \mathbf{y}_{\ell,m}(\boldsymbol{x}_{j,k}) + \tilde{\mathrm{v}}_{j,\ell,m} \mathbf{z}_{\ell,m}(\boldsymbol{x}_{j,k})\right) = \mathrm{v}_{j,k},
\end{aligned}$$

thus proving (IV.6), which completes the proof. □

Equations (IV.5) and (IV.6) show the needlet transform for consecutive levels. Recursively using (IV.5) and (IV.6) one obtains the *multi-level needlet transforms*.

B. Fast algorithms for tensor needlet transforms

In this section, we give the connection of needlet transforms and discrete Fourier transforms for vector spherical harmonics. It provides fast implementation of the needlet transforms with the computational steps that are nearly proportional to the size of input data or the number of the needlet coefficients at the finest level .

For $j \in \mathbb{N}_0$, we define the *discrete Fourier transform* $\mathbf{F}_j : l(\Lambda_j) \to l(N_j)$ for two sequences $\mathsf{b} := \{\mathsf{b}_{\ell,m} : \ell \in \mathbb{N},\ m = -\ell, \ldots, \ell\}$ in $l(\Lambda_j)$ and $\mathsf{c} := \{\mathsf{c}_{\ell,m} : \ell \in \mathbb{N},\ m = -\ell, \ldots, \ell\}$ in $l(\Lambda_j)$ as

$$\left(\mathbf{F}_j(\mathsf{b}, \mathsf{c})\right)_k := \sqrt{\omega_{j,k}} \sum_{\ell=0}^{\Lambda_j} \sum_{m=-\ell}^{\ell} \left(\mathsf{b}_{\ell,m}\, \mathbf{y}_{\ell,m}(\boldsymbol{x}_{j,k}) + \mathsf{c}_{\ell,m}\, \mathbf{z}_{\ell,m}(\boldsymbol{x}_{j,k})\right), \quad k = 0, \ldots, N_j$$

The sequence $\mathbf{F}_j(\mathsf{b},\mathsf{c})$ is called a pair of (Λ_j, N_j)-*sequences*, and the pair (b,c) is the sequences of *discrete Fourier coefficients* of $\mathbf{F}_j(\mathsf{b},\mathsf{c})$. Let $l(\Lambda_j, N_j)$ be the set of all (Λ_j, N_j)-pairs. The *adjoint discrete Fourier transform* $\mathbf{F}_j^* : l(N_j) \to l(\Lambda_j)$ for a sequence $\mathrm{v} = (\mathrm{v}_k)_{k=0}^{N_j} \in l(N_j)$ is

$$(\mathbf{F}_j^*\mathrm{v})_{\ell,m} := \left(\sum_{k=0}^{N_j} \mathrm{v}_k \sqrt{\omega_{j,k}}\, \overline{\mathbf{y}_{\ell,m}(\boldsymbol{x}_{j,k})}, \sum_{k=0}^{N_j} \mathrm{v}_k \sqrt{\omega_{j,k}}\, \overline{\mathbf{z}_{\ell,m}(\boldsymbol{x}_{j,k})} \right), \quad \ell = 0,\dots,\Lambda_j,\ m = -\ell,\dots,\ell.$$

Since $\mathcal{Q}_{N_j}$ is a polynomial-exact quadrature rule of degree 2^j, for every (Λ_j, N_j)-sequence v, there is a unique pair of sequences $\mathsf{b},\mathsf{c} \in l(\Lambda_j)$ such that $\mathbf{F}_j(\mathsf{b},\mathsf{c}) = \mathrm{v}$. We can write $(\hat{\mathrm{v}},\tilde{\mathrm{v}}) := (\mathsf{b},\mathsf{c}) = \mathbf{F}_j^*\mathrm{v}$ for the discrete Fourier coefficient sequence of a (Λ_j, N_j)-sequence v. Since $\widehat{(\mathrm{v} *_j h)}_{\ell m} = \hat{\mathrm{v}}_{\ell m}\, \widehat{h}\left(\frac{\lambda_\ell}{2^j}\right)$ and $\widetilde{(\mathrm{v} *_j h)}_{\ell m} = \tilde{\mathrm{v}}_{\ell m}\, \widehat{h}\left(\frac{\lambda_\ell}{2^j}\right)$ for $\ell \in \Lambda_j$ and $m = -\ell,\dots,\ell$, we obtain that $\widehat{\mathrm{v} *_j h}, \widetilde{\mathrm{v} *_j h} \in l(\Lambda_j)$ and the discrete convolution in (IV.1) is equivalent to $\mathbf{F}_j(\widehat{\mathrm{v} *_j h}, \widetilde{\mathrm{v} *_j h})$.

We can rewrite (IV.5) and (IV.6) using discrete Fourier transforms for vector spherical harmonics, as follows:

$$\begin{aligned}
&\mathrm{v}_{j-1} = (\mathrm{v}_j *_j a^\star)\downarrow_j = \mathbf{F}_{j-1}(\widehat{\mathrm{v}_j *_j a^\star}, \widetilde{\mathrm{v}_j *_j a^\star}),\\
&\mathrm{w}_{j-1}^n = \mathrm{v}_j *_j (b_n)^\star = \mathbf{F}_{j-1}(\widehat{\mathrm{v}_j *_j (b_n)^\star}, \widetilde{\mathrm{v}_j *_j (b_n)^\star}), \quad n = 1,\dots,r;\\
&(\mathbf{F}_j^*\mathrm{v}_j) = \left(\mathbf{F}_j^*(\mathrm{v}_{j-1})\right)\widehat{a} + \sum_{n=1}^{r} \left(\mathbf{F}_j^*(\mathrm{w}_{j-1}^n)\right)\widehat{b_n}.
\end{aligned} \tag{IV.7}$$

The following pseudo-code shows detailed implementation for the decomposition and reconstruction of multi-level FNTs.

Algorithm 1: Decomposition of Multi-Level FNT

Input : v_J – a (Λ_J, N_J)-sequence

Output: $\left(\{\mathrm{w}_{J-1}^n, \mathrm{w}_{J-2}^n, \dots, \mathrm{w}_{J_0}^n\}_{n=1}^r, \mathrm{v}_{J_0}\right)$

$\mathrm{v}_J \longrightarrow (\hat{\mathrm{v}}_J, \tilde{\mathrm{v}}_J)$ // adjoint FFT

for $j \leftarrow J$ **to** $J_0 + 1$ **do**

  $(\hat{\mathrm{v}}_{j-1}, \tilde{\mathrm{v}}_{j-1}) \longleftarrow (\hat{\mathrm{v}}_{j,\cdot}\, \overline{\widehat{a}}\,(2^{-j}\lambda_\cdot), \tilde{\mathrm{v}}_{j,\cdot}\, \overline{\widehat{a}}\,(2^{-j}\lambda_\cdot))$ // downsampling & convolution

  for $n \leftarrow 1$ **to** r **do**

    $(\hat{\mathrm{w}}_{j-1}^n, \tilde{\mathrm{w}}_{j-1}^n) \longleftarrow (\hat{\mathrm{v}}_{j,\cdot}\, \overline{\widehat{b_n}}\,(2^{-j}\lambda_\cdot), \tilde{\mathrm{v}}_{j,\cdot}\, \overline{\widehat{b_n}}\,(2^{-j}\lambda_\cdot))$ // convolution

    $\mathrm{w}_{j-1}^n \longleftarrow (\hat{\mathrm{w}}_{j-1}^n, \tilde{\mathrm{w}}_{j-1}^n)$ // FFT

  end

end

$\mathrm{v}_{J_0} \longleftarrow (\hat{\mathrm{v}}_{J_0}, \tilde{\mathrm{v}}_{J_0})$ // FFT

Algorithm 2: Reconstruction of Multi-Level FNT

Input : $\left(\{\mathrm{w}_{J-1}^n, \mathrm{w}_{J-2}^n, \ldots, \mathrm{w}_{J_0}^n\}_{n=1}^r, \mathrm{v}_{J_0}\right)$

Output: v_J – a (Λ_J, N_J)-sequence

$(\hat{\mathrm{v}}_{J_0}, \tilde{\mathrm{v}}_{J_0}) \longleftarrow \mathrm{v}_{J_0}$ // adjoint FFT

for $j \leftarrow J_0 + 1$ **to** J **do**

  for $n \leftarrow 1$ **to** r **do**

    $(\hat{\mathrm{w}}_{j-1}^n, \tilde{\mathrm{w}}_{j-1}^n) \longleftarrow \mathrm{w}_{j-1}^n$ // adjoint FFT

  end

  $\hat{\mathrm{v}}_j \longleftarrow \hat{\mathrm{v}}_{j-1,\cdot}\, \widehat{a}\,(2^{-j}\lambda_\cdot) + \sum_{n=1}^r \hat{\mathrm{w}}_{j-1,\cdot}^n\, \widehat{b_n}\,(2^{-j}\lambda_\cdot)$

  $\tilde{\mathrm{v}}_j \longleftarrow \tilde{\mathrm{v}}_{j-1,\cdot}\, \widehat{a}\,(2^{-j}\lambda_\cdot) + \sum_{n=1}^r \tilde{\mathrm{w}}_{j-1,\cdot}^n\, \widehat{b_n}\,(2^{-j}\lambda_\cdot)$ // upsampling & convolution

end

$\mathrm{v}_J \longleftarrow (\hat{\mathrm{v}}_J, \tilde{\mathrm{v}}_J)$ // FFT

C. Fast vector spherical harmonic transforms

Using the spherical coordinates, the scalar spherical harmonics can be explicitly written as, for $\ell = 0, 1, \ldots,$

$$Y_{\ell,m}(\boldsymbol{x}) := Y_{\ell,m}(\theta,\varphi) := \sqrt{\frac{2\ell+1}{4\pi}\frac{(\ell-m)!}{(\ell+m)!}}P_\ell^{(m)}(\cos\theta)\, e^{\mathrm{i}m\varphi}, \quad m = 0, 1, \ldots, \ell,$$
$$Y_{\ell,m}(\boldsymbol{x}) := (-1)^m Y_{\ell,-m}(\boldsymbol{x}), \quad m = -\ell, \ldots, -1.$$

In the following, we would suppress the variable $\boldsymbol{x}$ in $Y_{\ell,m} := Y_{\ell,m}(\boldsymbol{x})$ if no confusion arises.

Given the covariant spherical basis vectors [34],

$$\mathbf{e}_{+1} = -\frac{1}{\sqrt{2}}([1,0,0] + i[0,1,0])^T, \quad \mathbf{e}_0 = [0,0,1]^T, \quad \mathbf{e}_{-1} = \frac{1}{\sqrt{2}}([1,0,0] - i[0,1,0])^T, \tag{IV.8}$$

the *divergence-free* and *curl-free vector spherical harmonics* can be represented respectively as follows,

$$\begin{aligned} \mathbf{y}_{\ell,m} &= B_{+1,\ell,m}\mathbf{e}_{+1} + B_{0,\ell,m}\mathbf{e}_0 + B_{-1,\ell,m}\mathbf{e}_{-1}, \\ \mathbf{z}_{\ell,m} &= D_{+1,\ell,m}\mathbf{e}_{+1} + D_{0,\ell,m}\mathbf{e}_0 + D_{-1,\ell,m}\mathbf{e}_{-1}, \end{aligned} \tag{IV.9}$$

where $\lambda_\ell := \ell(\ell+1)$ is the eigenvalue of the Laplace-Beltrami operator Δ^* for $Y_{\ell,m}$ and the associated coefficients are explicitly given by

$$\begin{aligned} B_{+1,\ell,m} &= c_\ell C_{\ell-1,m-1,1,1}^{\ell,m} Y_{\ell-1,m-1} + d_\ell C_{\ell+1,m-1,1,1}^{\ell,m} Y_{\ell+1,m-1} \\ B_{0,\ell,m} &= c_\ell C_{\ell-1,m,1,0}^{\ell,m} Y_{\ell-1,m} + d_\ell C_{\ell+1,m,1,0}^{\ell,m} Y_{\ell+1,m} \\ B_{-1,\ell,m} &= c_\ell C_{\ell-1,m+1,1,-1}^{\ell,m} Y_{\ell-1,m+1} + d_\ell C_{\ell+1,m+1,1,-1}^{\ell,m} Y_{\ell+1,m+1} \\ D_{+1,\ell,m} &= iC_{\ell,m-1,1,1}^{\ell,m} Y_{\ell,m-1}, \\ D_{0,\ell,m} &= iC_{\ell,m,1,0}^{\ell,m} Y_{\ell,m}, \\ D_{-1,\ell,m} &= iC_{\ell,m+1,1,-1}^{\ell,m} Y_{\ell,m+1}, \end{aligned} \tag{IV.10}$$

where the Clebsch-Gordan (CG) coefficients

$$C^{\ell,m}_{j_1,m_1,j_2,m_2} := (-1)^{(m+j_1-j_2)}\sqrt{2\ell+1}\begin{pmatrix} j_1 & j_2 & \ell \\ m_1 & m_2 & -m \end{pmatrix},$$

and

$$c_\ell := \sqrt{\frac{\ell+1}{2\ell+1}}, \quad d_\ell := \sqrt{\frac{\ell}{2\ell+1}}. \tag{IV.11}$$

The Clebsch-Gordan coefficients are most familiar in quantum mechanics as the coefficients of a unitary transformation that connects the tensor product basis from irreducible representations of SO(3), to its irreducible components in a direct sum, labelled by total angular momentum invariants [34], [35]. However, the more abstract algebraic theory of algebraic invariants by Clebsch and Gordon, was developed earlier in the 19th Century [36].

By (IV.8) and (IV.9), for $\ell \geq 1, m = -\ell, \ldots, \ell$, the divergence-free and curl-free vector spherical harmonics of degree (ℓ, m) are

$$\mathbf{y}_{\ell,m} = \begin{pmatrix} -\frac{1}{\sqrt{2}}\left(B_{+1,\ell,m} - B_{-1,\ell,m}\right) \\ -\frac{1}{\sqrt{2}}\mathrm{i}\left(B_{+1,\ell,m} + B_{-1,\ell,m}\right) \\ B_{0,\ell,m} \end{pmatrix} \qquad \mathbf{z}_{\ell,m} = \begin{pmatrix} -\frac{1}{\sqrt{2}}\left(D_{+1,\ell,m} - D_{-1,\ell,m}\right) \\ -\frac{1}{\sqrt{2}}\mathrm{i}\left(D_{+1,\ell,m} + D_{-1,\ell,m}\right) \\ D_{0,\ell,m} \end{pmatrix}. \tag{IV.12}$$

The set of vector spherical harmonics $\{\mathbf{y}_{\ell,m}, \mathbf{z}_{\ell,m} : \ell = 1, 2, \ldots, m = -\ell, \ldots, \ell\}$ which is used in quantum mechanics [34] forms an orthonormal basis for $\mathbf{L}_2(\mathbb{S}^2)$. Based on properties detailed in [37], we can obtain the explicit expression of those (CG) coefficients, respectively, see details in [30].

By (IV.12), we can obtain that fast vector spherical harmonics transforms can be produced by implementing FFT and also adjoint FFT on scalar spherical harmonics several times [2], [38]–[41]. Due to the space limitation, we suggest the readers to refer to [30] for more technical details.

D. Computational complexity analysis

In the relation (IV.7) the discrete convolution has the computational steps $\mathcal{O}(N_j)$ for level j. FFTs for vector spherical harmonics have computational complexity $\mathcal{O}\left(N\sqrt{\log N}\right)$ for input data of size N, $N \geq 1$. For decomposition and reconstruction in (IV.7), the input data has length up to N_J. Thus, the computational cost of the needlet transforms, which would be dominated by those of FFTs, is $\mathcal{O}(N_J)$. Hence, we call the needlet transforms in (IV.7) and their multi-level versions *fast needlet transforms* or *FNTs* for vector fields on $\mathbb{S}^2$.

V. Numerical Study

In this section, we start with an explicit construction of tensor needlets on $\mathbb{S}^2$, then introduce two types of quadrature rule nodes and three kinds of vector fields used in our experiments. Later, we describe the experimental setup for using FNTs in our simulations. After that, one real-world wind field is used as a case study. We present the simulation results on these vector fields and discuss the effectiveness and efficiency of our proposed method.

A. *Tensor needlets construction*

Here we demonstrate the procedures of tensor needlets construction, as similar to the steps performed in [23]. Based on our theoretical results, the construction needs several components: an explicit formulation of filter banks and the associated generators, vector spherical harmonics and a set of quadrature rule nodes for the discretization of continuous integral.

First, for the filter bank, let us consider a simple one with two high-pass filters, that is, $\boldsymbol{\eta} = \{a; b_1, b_2\}$, with the Fourier series denoted by

$$\widehat{a}(\xi) := \begin{cases} 1, & |\xi| < \frac{1}{8}, \\ \cos\big(\frac{\pi}{2}\nu(8|\xi|-1)\big), & \frac{1}{8} \le |\xi| \le \frac{1}{4}, \\ 0, & \frac{1}{4} < |\xi| \le \frac{1}{2}, \end{cases}$$

$$\widehat{b_1}(\xi) := \begin{cases} 0, & |\xi| < \frac{1}{8}, \\ \sin\big(\frac{\pi}{2}\nu(8|\xi|-1)\big), & \frac{1}{8} \le |\xi| \le \frac{1}{4}, \\ \cos\big(\frac{\pi}{2}\nu(4|\xi|-1)\big), & \frac{1}{4} < |\xi| \le \frac{1}{2}. \end{cases}$$

$$\widehat{b_2}(\xi) := \begin{cases} 0, & |\xi| < \frac{1}{4}, \\ \sin\big(\frac{\pi}{2}\nu(4|\xi|-1)\big), & \frac{1}{4} \le |\xi| \le \frac{1}{2}, \end{cases}$$

where

$$\nu(t) := \chi_3(t)^2 = t^4(35 - 84t + 70t^2 - 20t^3), \quad t \in \mathbb{R},$$

as in [17, Chapter 4]. It holds that for all $\xi \in [0, 1/2]$, $|\widehat{a}(\xi)|^2 + |\widehat{b_1}(\xi)|^2 + |\widehat{b_2}(\xi)|^2 = 1$, which implies (III.18). Therefore, the associated generators $\Psi = \{\alpha; \beta^1, \beta^2\}$ that satisfy (III.3) and (III.9) can be explicitly defined by

$$\widehat{\alpha}(\xi) = \begin{cases} 1, & |\xi| < \frac{1}{4}, \\ \cos\big(\frac{\pi}{2}\nu(4|\xi|-1)\big), & \frac{1}{4} \le |\xi| \le \frac{1}{2}, \\ 0, & \text{else}, \end{cases}$$

$$\widehat{\beta^1}(\xi) = \begin{cases} \sin\left(\frac{\pi}{2}\nu(4|\xi|-1)\right), & \frac{1}{4} \le |\xi| < \frac{1}{2}, \\ \cos^2\left(\frac{\pi}{2}\nu(2|\xi|-1)\right), & \frac{1}{2} \le |\xi| \le 1, \\ 0, & \text{else}, \end{cases}$$

$$\widehat{\beta^2}(\xi) = \begin{cases} 0, & |\xi| < \frac{1}{2}, \\ \cos\left(\frac{\pi}{2}\nu(2|\xi|-1)\right)\sin\left(\frac{\pi}{2}\nu(2|\xi|-1)\right), & \frac{1}{2} \le |\xi| \le 1, \\ 0, & \text{else}. \end{cases}$$

Then, $\widehat{a}, \widehat{b_1}, \widehat{b_2}, \widehat{\alpha}, \widehat{\beta^1}, \widehat{\beta^2}$ are all in $C^{4-\epsilon}(\mathbb{R})$ for some small positive ϵ [17, p. 119], $\operatorname{supp}\widehat{\alpha} \subseteq [0, 1/2]$ and $\operatorname{supp}\widehat{\beta^n} \subseteq [1/4, 1]$, $n = 1, 2$. Also, the refinable function $\widehat{\alpha}$ satisfies (III.17). We omit the visualization of the filters $\widehat{a}$, $\widehat{b_1}$, $\widehat{b_2}$ and the functions $\widehat{\alpha}$, $\widehat{\beta^1}$, $\widehat{\beta^2}$. Readers can refer to [23] for the plotting.

The continuous tensor needlets $\mathbf{\Phi}_{j,\boldsymbol{y}}(\boldsymbol{x})$, $\mathbf{\Psi}^1_{j,\boldsymbol{y}}(\boldsymbol{x})$ and $\mathbf{\Psi}^2_{j,\boldsymbol{y}}(\boldsymbol{x})$ on $\mathbb{S}^2$ are expressed by

$$\mathbf{\Phi}_{j,\boldsymbol{y}}(\boldsymbol{x}) := \sum_{\ell=1}^{\infty} \widehat{\alpha}\left(\frac{\ell}{2^j}\right) \sum_{m=-\ell}^{\ell} \Big(\mathbf{y}_{\ell,m}(\boldsymbol{x}) \otimes \mathbf{y}_{\ell,m}(\boldsymbol{y}) + \mathbf{z}_{\ell,m}(\boldsymbol{x}) \otimes \mathbf{z}_{\ell,m}(\boldsymbol{y})\Big),$$

$$\mathbf{\Psi}^n_{j,\boldsymbol{y}}(\boldsymbol{x}) := \sum_{\ell=1}^{\infty} \widehat{\beta^n}\left(\frac{\ell}{2^j}\right) \sum_{m=-\ell}^{\ell} \Big(\mathbf{y}_{\ell,m}(\boldsymbol{x}) \otimes \mathbf{y}_{\ell,m}(\boldsymbol{y}) + \mathbf{z}_{\ell,m}(\boldsymbol{x}) \otimes \mathbf{z}_{\ell,m}(\boldsymbol{y})\Big), \quad n = 1, \ldots, 2,$$

where the vector spherical harmonics $\mathbf{y}_{\ell,m}$, $\mathbf{z}_{\ell,m}$ are defined in (IV.9).

Based on Theorem III.2 and the construction of Ψ and $\boldsymbol{\eta}$ in (V.2) and (V.1), one can easily verify that the continuous tensor needlet system $\mathsf{CFS}_J(\Psi) = \{\mathbf{\Phi}_{J,\boldsymbol{y}}; \mathbf{\Psi}^1_{j,\boldsymbol{y}}, \mathbf{\Psi}^2_{j,\boldsymbol{y}} : j \geq J, \boldsymbol{y} \in \mathbb{S}^2\}$ on $\mathbb{S}^2$ is a tight tensor needlet system for $L_2(\mathbb{S}^2)$ for any $J \in \mathbb{Z}$.

By using a polynomial-exact quadrature rule $\mathcal{Q}_{N_j}$ on $\mathbb{S}^2$, we can obtain the discrete framelets $\mathbf{\Phi}_{j,k}(\boldsymbol{x})$, $\mathbf{\Psi}^1_{j,k}(\boldsymbol{x})$ and $\mathbf{\Psi}^2_{j,k}(\boldsymbol{x})$, that is

$$\mathbf{\Phi}_{j,k}(\boldsymbol{x}) := \sqrt{\omega_{j,k}} \sum_{\ell=1}^{\infty} \widehat{\alpha}\left(\frac{\lambda_\ell}{2^j}\right) \sum_{m=-\ell}^{\ell} \left(\mathbf{y}_{\ell,m}(\boldsymbol{x}) \otimes \mathbf{y}_{\ell,m}(\boldsymbol{x}_{j,k}) + \mathbf{z}_{\ell,m}(\boldsymbol{x}) \otimes \mathbf{z}_{\ell,m}(\boldsymbol{x}_{j,k})\right),$$

$$\mathbf{\Psi}^n_{j,k'}(\boldsymbol{x}) := \sqrt{\omega_{j+1,k'}} \sum_{\ell=1}^{\infty} \widehat{\beta^n}\left(\frac{\lambda_\ell}{2^j}\right) \sum_{m=-\ell}^{\ell} \left(\mathbf{y}_{\ell,m}(\boldsymbol{x}) \otimes \mathbf{y}_{\ell,m}(\boldsymbol{x}_{j+1,k'}) + \mathbf{z}_{\ell,m}(\boldsymbol{x}) \otimes \mathbf{z}_{\ell,m}(\boldsymbol{x}_{j+1,k'})\right).$$

Then, we have $\mathbf{\Phi}_{j,k} \in \Pi_{2^{j-1}}$ and $\mathbf{\Psi}^1_{j,k}, \mathbf{\Psi}^2_{j,k} \in \Pi_{2^j}$ because that the supports of $\widehat{\alpha}$, $\widehat{\beta^1}$ and $\widehat{\beta^2}$ are subsets of $[0, 1/2]$, $[0, 1]$ and $[0, 1]$. Given $\mathcal{Q}_{N_j}$ a polynomial-exact quadrature rule of degree 2^j for all $j \in \mathbb{Z}$, the tensor needlet system $\mathsf{FS}_J(\boldsymbol{\eta}; \{\mathcal{Q}_{N_j}\}_{j \geq J}) := \{\mathbf{\Phi}_{J,k}; \mathbf{\Psi}^1_{j,k'}, \mathbf{\Psi}^2_{j,k'} : j \geq J,\ k = 1, \ldots, N_J,\ k' = 1, \ldots, N_{j+1}\}$ is a semi-discrete tight needlet system for $L_2(\mathbb{S}^2)$ for all $J \in \mathbb{Z}$.

B. Data points

In our experiments, we consider two types of polynomial-exact quadrature rule point sets, described as follows

1) *Gauss-Legendre tensor product rule* (GL) [42]. The Gauss-Legendre tensor product rule is a (polynomial-exact but not equal area) quadrature rule $\mathcal{Q}_{N_j} := \{(w_i, \mathbf{x}_i)\}_{i=1}^N, i = 0, \ldots, N\}$ on the sphere generated by the tensor product of the Gauss-Legendre nodes on the interval $[-1, 1]$ and equi-spaced nodes on the longitude with non-equal weights. Figure 1(a) shows $N = 512$ GL points.
2) *Symmetric spherical designs* (SD) [43]. The symmetric spherical design is a (polynomial-exact) quadrature rule $\mathcal{Q}_{N_j} := \{(w_i, \mathbf{x}_i)\}_{i=1}^N, i = 0, \ldots, N\}$ on the sphere $\mathbb{S}^2$ with equal weights $w_i = 1/N$. The points are "equally" distributed on the sphere. Figure 1(b) shows $N = 498$ SD points.

C. Synthetic vector fields on $\mathbb{S}^2$

To verify our theoretical results and the proposed algorithms, we use three types of simulated vector fields provided in [1]. All these fields are generated using "stream functions" and "velocity potentials" so that we can easily separate the divergence-free and curl-free parts of the field. Denoted by s and v the stream function and velocity potential, respectively, then each of the vector fields can be represented by

$$T = \underbrace{\mathbf{L}s}_{f^{\text{div}}} + \underbrace{\nabla_* v}_{f^{\text{curl}}}.$$

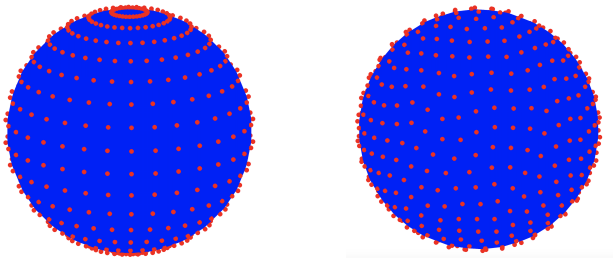

(a) GL, $N = 512$ **(b)** SD, $N = 498$

Fig. 1: Point sets on the sphere for: (a) Nodes of Gauss-Legendre tensor rule (GL), (b) Nodes of symmetric spherical designs (SD)

Recall from Section 2 that $\mathbf{L}$ and ∇_* denote the surface curl and surface gradient, respectively. Therefore, $\mathbf{L}s$ is divergent-free while $\nabla_* v$ is curl-free.

Now we detail the formulation of these two vector fields one-by-one.

Vector Field 1. The stream function and velocity potential for this field are linear combinations of spherical harmonics and are meant to generate realistic synoptic scale meteorological wind fields [1].

The stream function is defined by

$$s_1(\boldsymbol{x}) = -\frac{1}{\sqrt{3}} Y_{1,0}(\boldsymbol{x}) + \frac{8\sqrt{2}}{3\sqrt{385}} Y_{5,4}(\boldsymbol{x}), \tag{V.3}$$

which is known as a Rosby–Haurwitz wave and is an analytic solution to the nonlinear barotropic vorticity equation on the sphere [4, pp. 453–454]. In [44], s_1 was used as the initial condition for one of the de facto test cases for the shallow water wave equations on the sphere.

The velocity potential is given by

$$v_1(\boldsymbol{x}) = \frac{1}{25}(Y_{4,0}(\boldsymbol{x}) + Y_{6,-3}(\boldsymbol{x})).$$

We can choose different orders of the the spherical harmonics (l, m) and coefficients in the above formulation of scalar potentials. Here, we have used the same setting as [1].

Vector Field 2. This field still uses the Rosby–Haurwitz wave (V.3) as the stream function, while a linear combination of compactly supported functions for the velocity potential, i.e.,

$$v_2(\boldsymbol{x}) = \frac{1}{8} f(\boldsymbol{x}; 5, \pi/6, 0) - \frac{1}{7} f(\boldsymbol{x}; 3, \pi/5, \pi/7) + \frac{1}{9} f(\boldsymbol{x}; 5, -\pi/6, \pi/2) - \frac{1}{8} f(\boldsymbol{x}; 3, -\pi/5, \pi/3)$$

where

$$f(\boldsymbol{x}; \sigma, \theta_c, \lambda_c) = \frac{\sigma^3}{12} \sum_{j=0}^{4} (-1)^j \begin{pmatrix} 4 \\ j \end{pmatrix} \left| r - \frac{(j-2)}{\sigma} \right|^3$$

Vector Field 3. Let $\boldsymbol{x}_c \in S^2$ have spherical coordinates (θ_c, λ_c), and let $t = \boldsymbol{x} \cdot \boldsymbol{x}_c$ and $a = 1 - t$. Define

$$g(\boldsymbol{x}; \theta_c, \lambda_c) = -\frac{1}{2}((3t + 3\sqrt{2}a^{3/2} - 4) + (3t^2 - 4t + 1)\log(a) + (3t - 1)a\log(\sqrt{2a} + a))$$

The stream function for this vector field is given by:

$$s_3(x) = \int_{-\pi/2}^{\theta} \sin^{14}(2\xi) d\xi - 3g(x; \pi/4, -\pi/12),$$

where θ denotes the latitudinal coordinate of $\boldsymbol{x}$.

The velocity potential is also defined using g as follows:

$$v_3(\boldsymbol{x}) = \frac{5}{2}g(\boldsymbol{x}; \pi/4, 0) - \frac{7}{4}g(\boldsymbol{x}; \pi/6, \pi, 9) - \frac{3}{2}g(\boldsymbol{x}; 5\pi/16, \pi/10).$$

The left columns of Figure 2 and 3 present the vector fields sampled at $N = 2178$ GL points and $N = 2148$ SD points, respectively.

D. Experimental setup

Based on the developed theoretical results and methodology, we detail the main steps performed in the experimental study. First, in order to precess the simulated vector fields by means of Algorithm 1 and 2, we need to construct a semi-discrete tensor needlets system given by (III.15), where $\Psi = \{\alpha; \beta^1, \beta^2\}$ are the generators associated with the filter bank $\boldsymbol{\eta} = \{a; b_1, b_2\}$ introduced in subsection V-A, $\mathcal{Q}_{N_j}$ is a sequence of quadrature rule point sets (GL or SD). To satisfy the requirements of the implementations of decomposition and reconstruction algorithm, the data sequence v sampled from the vector fields on $\mathcal{Q}_{N_J}$ (at the finest scale J) must be a (Λ_j, N_j)-sequence. For this purpose, we can project v onto Π_{2^J} by performing $\mathrm{v}_J = (\mathbf{F}_J^* \mathbf{F}_J)^{-1} \mathbf{F}_J^* \mathrm{v}$, where $\mathbf{F}_J$ and $\mathbf{F}_J^*$ can be implemented fast by the forward FaVeST and adjoint FaVeST [30], respectively. In this manner, we obtain an approximation coefficient sequence v_J at the finest scale (i.e., a (Λ_j, N_j)-sequence) and the projection error sequence $\widetilde{\mathrm{w}}_J = \mathrm{v} - \mathrm{v}_J$.

Recall that GL/SD is a (polynomial-exact) quadrature rule of order 2^j for all $j = J_0, \ldots, J$. Therefore, based on Theorem IV.1, we can implement decomposition of FNT (Algorithm 1) on the (Λ_J, N_J)-sequence v_J and obtain the coefficient sequences w_{J-1}^1, w_{J-1}^2, ..., $\mathrm{w}_{J_0}^1$, $\mathrm{w}_{J_0}^2$, v_{J_0}. Afterwards, we can exactly reconstruct v_J from the decomposed coefficient sequences $(\mathrm{w}_{J-1}^1, \ldots, \mathrm{w}_{J-1}^r, \ldots, \mathrm{w}_{J_0}^1, \ldots, \mathrm{w}_{J_0}^r, \mathrm{v}_{J_0})$ by using the reconstruction of FNT (Algorithm 2). Once v_J is obtained, the simulated data sequence $\mathrm{v} = \mathrm{v}_J + \widetilde{\mathrm{w}}_J$ will be constructed with the pre-computed projection error $\widetilde{\mathrm{w}}_J$.

E. Results and discussion

The middle columns of Figure 2 and 3 show the reconstruction of vector fields (i.e., T^{rec}) by one level FNT with $J_0 = 4, J = 5$. We have used $N = 2178$ GL points and $N = 2148$ SD points, respectively. The corresponding errors $T - T^{\mathrm{rec}}$ (on the sampled points) are visualized in the right columns. Also, the maximum norm of the target vector fields, the reconstructed vector fields, and the error fields are displayed for each case. It is clear that one level FNT works effectively on these vector fields. Reconstruction errors for vector field 1 (on either GL and SD points) are smaller than that of vector field 2 due to its better smoothness. For a better resolution, we only demonstrate the visualization of the case with $J = 5$.

Table I summarizes the relative l_2 reconstruction errors, i.e., $\|T - T^{\mathrm{rec}}\|_2 / \|T\|_2$ with GL and SD points for $J = 3, 4, \ldots, 7$ and $J_0 = J - 1$. In both GL and SD cases, the relative reconstruction error increases for each level J as the smoothness of the field decreases. This illustrates that the accuracy of the algorithm improves as the smoothness of the vector fields reduces. As expected, the reconstruction error becomes smaller if more quadrature rule points (e.g. higher level J) are provided. For these three vector fields, both options of quadrature points result in similar order of magnitudes in error. On the other hand, the obtained relative l_2 errors for these three vector fields match the accuracies made by SBFs interpolation

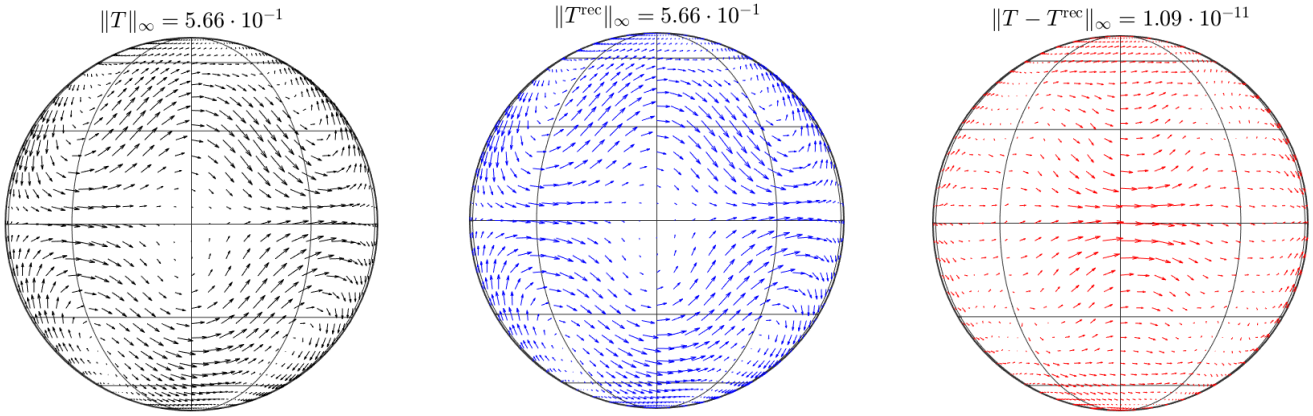

(a) Reconstruction of Vector Field 1 with GL points

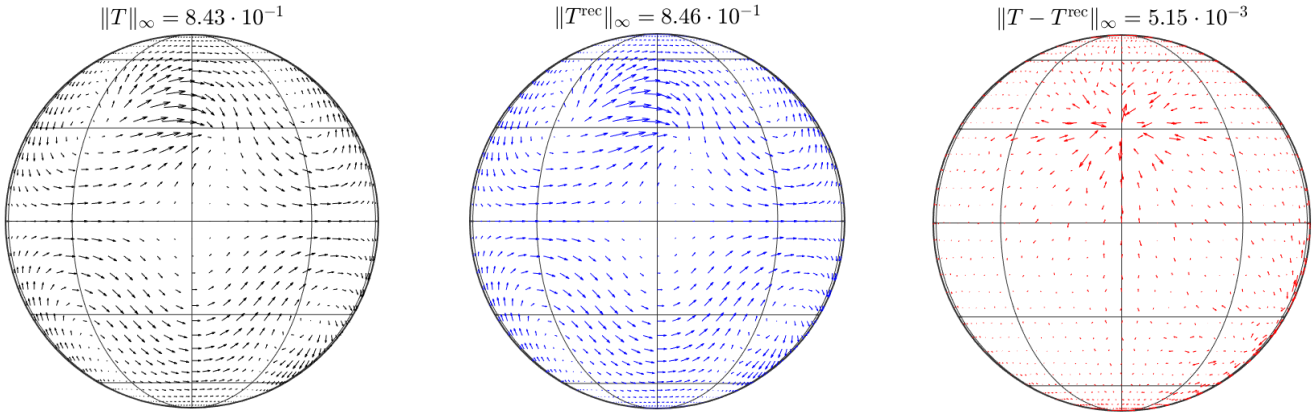

(b) Reconstruction of Vector Field 2 with GL points

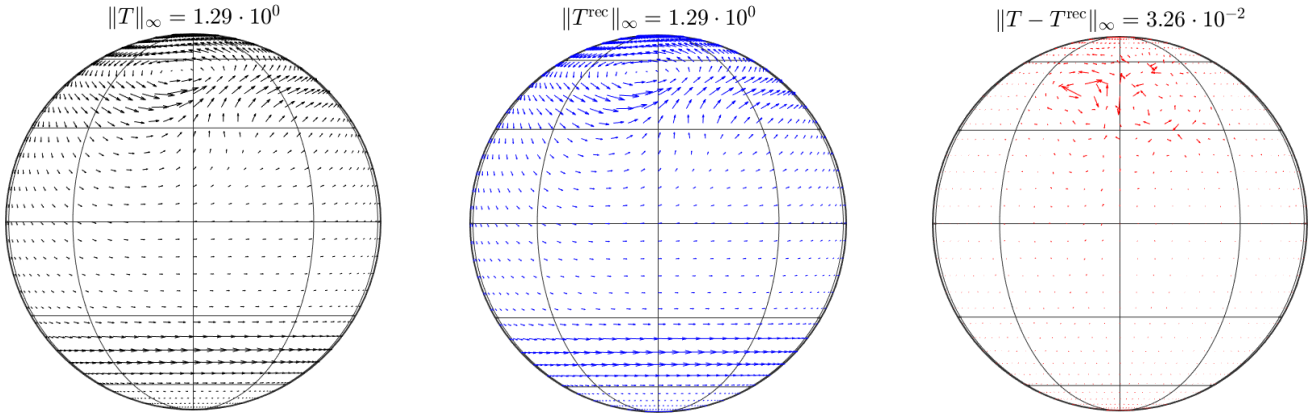

(c) Reconstruction of Vector Field 3 with GL points

Fig. 2: Visualization of the vector field reconstruction by one level FNT with GL points. The first column shows the target vector field T while the second and third columns correspond to the reconstruction T^{rec} and error $T - T^{\text{rec}}$, respectively. All plots are orthographic projections of the fields sampled at level $J = 5$ with $N = 2178$ GL nodes. The normalized max norms for T, T^{rec}, and $T - T^{\text{rec}}$ are displayed for each case.

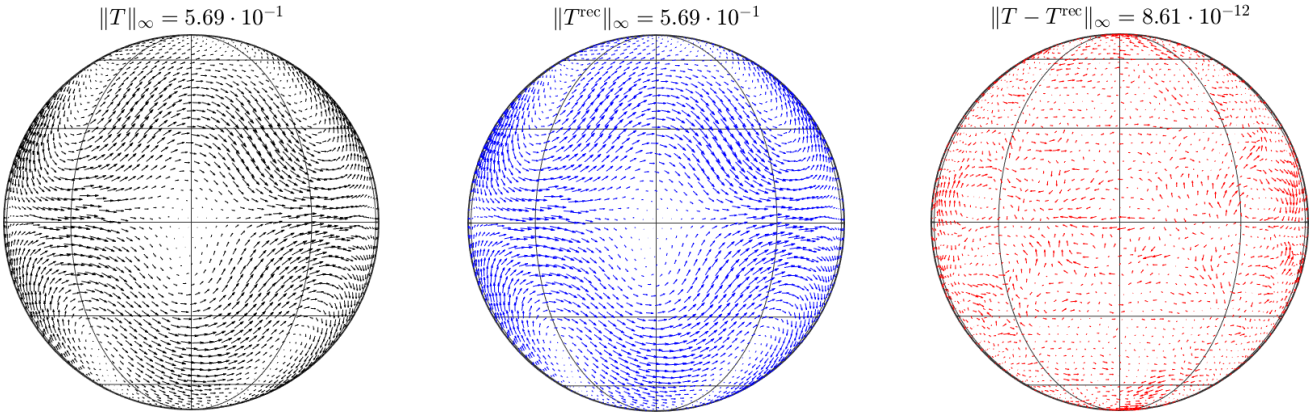

(a) Reconstruction of Vector Field 1 with SD points

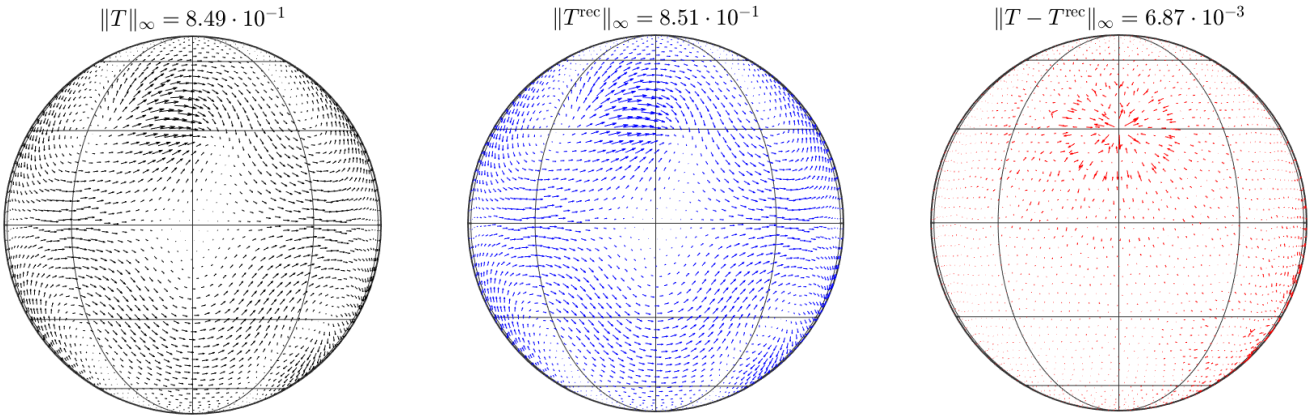

(b) Reconstruction of Vector Field 2 with SD points

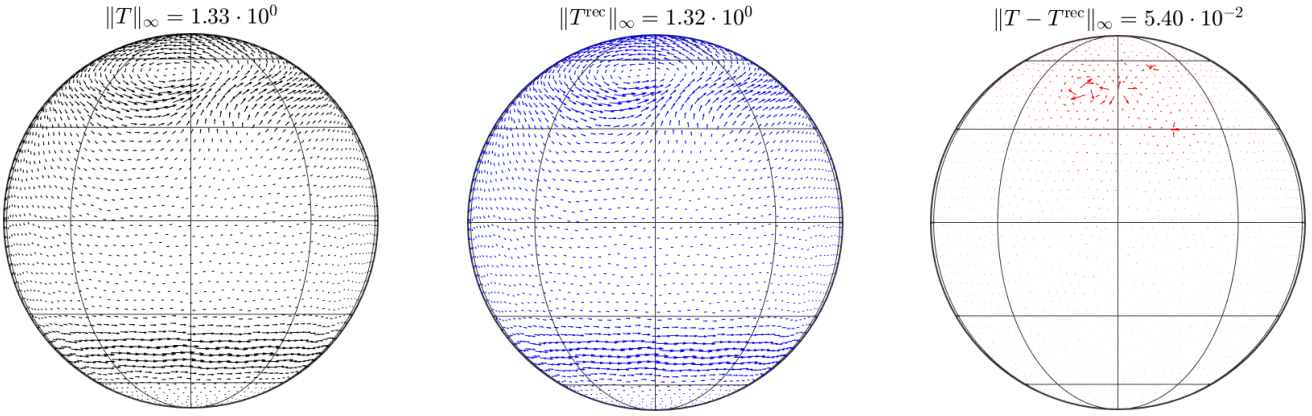

(c) Reconstruction of Vector Field 3 with SD points

Fig. 3: Visualization of the vector field reconstruction by one level FNT with SD points. The first column shows the target vector field T while the second and third columns correspond to the reconstruction T^{rec} and error $T - T^{\text{rec}}$, respectively. All plots are orthographic projections of the fields sampled at level $J = 5$ with $N = 2148$ SD nodes. The normalized max norms for T, T^{rec}, and $T - T^{\text{rec}}$ are displayed for each case.

as reported in [12]. For example, when $J = 6$, $N = 8450$ GL points ($N = 8388$ for SD) are used in the simulation, the reconstruction of FNT have accuracies $10^{-12} \sim 10^{-10}$, 10^{-4}, 10^{-3} for vector field 1,2, and 3, respectively. That coincides with the results presented in [12], e.g. the mesh-norm h_X is near 0.03 (when roughly 10,000 minimum energy (ME) nodes are used) and the associated relative errors also reach similar orders, as visualized in Figure 5 in [12]. Theoretical analysis for the estimation of approximation error rate of FNT is left for our future work.

	Points	$J = 3$	$J = 4$	$J = 5$	$J = 6$	$J = 7$
Vector Field 1	GL	1.5307e-11	1.5189e-11	1.3221e-11	9.4731e-12	7.7702e-12
	SD	3.4493e-10	7.8381e-12	7.1309e-12	5.9779e-12	2.9931e-10
Vector Field 2	GL	1.4251e-01	4.2991e-03	2.5075e-03	3.1045e-04	5.2139e-05
	SD	1.3980e-01	5.4539e-03	2.4392e-03	3.6280e-04	5.8053e-05
Vector Field 3	GL	2.3607e-01	4.1204e-02	4.5036e-03	1.1086e-03	2.9840e-04
	SD	2.4784e-01	3.2988e-02	4.8478e-03	1.3185e-03	3.5757e-04

TABLE I: Relative l_2 reconstruction errors $\|T - T^{\mathrm{rec}}\|_2/\|T\|_2$ with GL and SD quadrature nodes

To further test and illustrate the multiresolution decomposition and reconstruction of Algorithms 1 and 2. We conduct multi-level FNT on three synthetic vector fields with GL/SD points for $J_0 = 2, 3, 4, 5$ and $J = 6$. Table II reports the relative l_2 approximation error of approximation coefficient v_J, i.e., $\|\mathrm{v}_J - \mathrm{v}_J^{\mathrm{rec}}\|_2/\|\mathrm{v}_J\|_2$. They are determined by the approximation error of numerical integration by quadrature rule and the truncation error of vector spherical harmonic expansion. We sample the vector field 1 at GL points $\mathcal{Q}_J$ with level $J = 6$, to obtain the target data sequence v, as Figure 4 shows. Applying Algorithm 1, we obtain the projection v_6 and calculate projection error $\tilde{\mathrm{w}}_6 = \mathrm{v} - \mathrm{v}_6$. At the level $j = 5$, the projection v_6 can be decomposed into tensor needlet approximation coefficient sequence v_5 and two detail coefficient sequences w_5^1 and w_5^1. Correspondingly, the approximation coefficient sequence at level $j = 5$ can be decomposed into approximation coefficient sequence and two detail coefficient sequences at lower level $j = 4$. Figure 4 shows that Algorithm 1 works effectively in multiresolution analysis, by decomposing a projection at higher level to lower levels and providing a good approximation and detail coefficient sequences. Table II verifies that the multiresolution decomposition and reconstruction incur very small approximation error.

	Points	$J_0 = 5$	$J_0 = 4$	$J_0 = 3$	$J_0 = 2$
Vector Field 1	GL	6.6588e-12	8.1094e-12	5.4339e-12	1.0277e-11
	SD	3.6901e-12	3.9141e-12	3.5454e-12	3.4472e-10
Vector Field 2	GL	6.6199e-12	7.9541e-12	5.4505e-12	1.0124e-11
	SD	3.6367e-12	3.7764e-12	3.3577e-12	3.4327e-10
Vector Field 3	GL	1.0557e-11	8.9087e-12	6.7804e-12	9.9225e-12
	SD	3.2625e-12	3.6789e-12	3.1106e-12	8.2024e-10

TABLE II: Relative l_2 approximation error of approximation coefficient v_J: $\|\mathrm{v}_J - \mathrm{v}_J^{\mathrm{rec}}\|_2/\|\mathrm{v}_J\|_2$ with GL and SD quadrature nodes ($J = 6$)

To verify the time complexity of Algorithms 1 and 2, we conduct experiments for the multi-level FNT with GL points for $J = 5, 6, \ldots, 11$ and $J_0 = 1$. In the simulations $N := N_J \approx 2^{2J+1}$ GL nodes are used in the implementation of the multi-level FNT decomposition, and $M := M_J \approx 2^{2J}$ coefficients are used in the multi-level FNT reconstruction. For $J = 5, 6, \ldots, 11$, the CPU time cost by the FNT decomposition and reconstruction are summarized in Table III. It also displays the ratio of time cost between levels J and $J-1$ to reflect the increasing rate. Correspondingly, Figure 5(a) and (b) show the nearly linear complexity of the FNT decomposition and reconstruction, respectively. For example, the FNT decomposition is approximately of $\mathcal{N}^{1.1}$ complexity, and similarly the FNT reconstruction is of $\mathcal{M}^{1.1}$ complexity. Table III and Figure 5 are based on vector field 1. Our empirical studies show that similar results and conclusion are true for the other two vector fields. These numerical findings verify the efficiency of the FNT algorithms.

J	5	6	7	8	9	10	11
N	2,178	8,450	33,282	132,098	526,338	2,101,250	8,396,802
t^{dec}	0.1268	0.3196 (2.5)	0.8175 (2.6)	3.3465 (4.1)	15.7947 (4.7)	78.5736 (5.0)	445.8219 (5.7)
M	1,088	4,224	16,640	66,048	263,168	1,050,624	4,198,400
t^{rec}	0.0650	0.2165 (3.3)	0.5647 (2.6)	2.3386 (4.1)	10.7283 (4.6)	51.9840 (4.8)	284.9573 (5.5)

TABLE III: Multi-level FNT decomposition CPU time t^{fwd} v.s. number of points and multi-level FNT reconstruction CPU time (in seconds) t^{adj} v.s. number of coefficients $J_0 = 2$ and $5 \le J \le 11$. FNT decomposition uses Gauss-Legendre tensor rule which has $N = N_J \approx 2^{2J+1}$ nodes and FNT reconstruction uses $M = M_J \approx 2^{2J}$ coefficients. The numbers inside brackets are the ratios $\frac{t^{\mathrm{dec}}(N_J)}{t^{\mathrm{dec}}(N_{J-1})}$ and $\frac{t^{\mathrm{rec}}(M_J)}{t^{\mathrm{rec}}(M_{J-1})}$ for decomposition and for reconstruction, respectively . The numerical test was run under Intel Core i7-4770 CPU @ 3.40GHz with 16GB RAM in Windows 10.

F. Case study: Earth wind data analysis

In this subsection, we use a climatological wind field described in NCEP/NCAR Reanalysis [45] to test the effectiveness of the proposed FNT algorithms for real world earth wind data. It is common in meteorology to express the wind vector in terms of two orthogonal velocity components [46], [47], i.e.,

- u is the zonal velocity, i.e. the component of the horizontal wind towards east;
- v is the meridional velocity, i.e. the component of the horizontal wind towards north.

In this case study, we use the NCEP/NCAR Reanalysis daily average data available from the cite of Physical Sciences Division (PSD)*. In the simulations, we only consider the samples at year 2018 with the first pressure level (17 in total) and first time instant (205 in total). Its spatial coverage performs in 2.5 degree $\times$ 2.5 degree global grids (144$\times$73).

Based on Equation (16) in [48], we convert the wind field expressed in u and v to the 3D representation $T = [T_1, T_2, T_3]$. Then we sample the vector fields at GL points with $J = 6$, i.e., 8450 points satisfying the quadrature rule. It provides an approximation of the real wind field. In Figure 6, we plot the real wind field with 8450 GL samples, the reconstructed vector field by using one level FNT and the residual vector

*https://www.esrl.noaa.gov/psd/data/gridded/data.ncep.reanalysis.pressure.html

field, from left to right, respectively. For a better resolution, we only display the range with longitude in [100,250] (the actual range of the original earth wind is [0,357.5]) and latitude in [-60,60] (the actual range is [-90,90]). The (normalized) maximum norms, i.e., $\|T\|_\infty$, $\|T^{\rm rec}\|_\infty$ and $\|T - T^{\rm rec}\|_\infty/\|T\|_\infty$, in terms of 8450 samples, are displayed for each plot. It can be observed that FNT works effectively on reconstruction although the wind field changes rapidly in some region. On the other hand, the relative error l_2-error $\|T - T^{\rm rec}\|_2/\|T\|_2$ is 0.1380. It should be noted that the error magnitude is mainly caused by the approximation of original scattered instances with GL points, which can be viewed as 'data-preprocessing' error, and the approximation error induced by FNT algorithms, which is determined by the 'smoothness' of the real-world vector field. Actually, one can also conduct vector spherical basis function (SBF) interpolation [12] to obtain the approximated wind field with GL/SD samples, which indeed is outside of our primary focus in this work.

ACKNOWLEDGMENT

This research was partially supported under the Australian Research Council's Discovery Project DP160101366. We would thank E. J. Fuselier and G. B. Wright for providing their MATLAB codes implementing vector field examples. The case study for earth wind data analysis is based on NCEP Reanalysis data provided by the NOAA/OAR/ESRL PSD, Boulder, Colorado, USA, from their Web site at https://www.esrl.noaa.gov/psd/

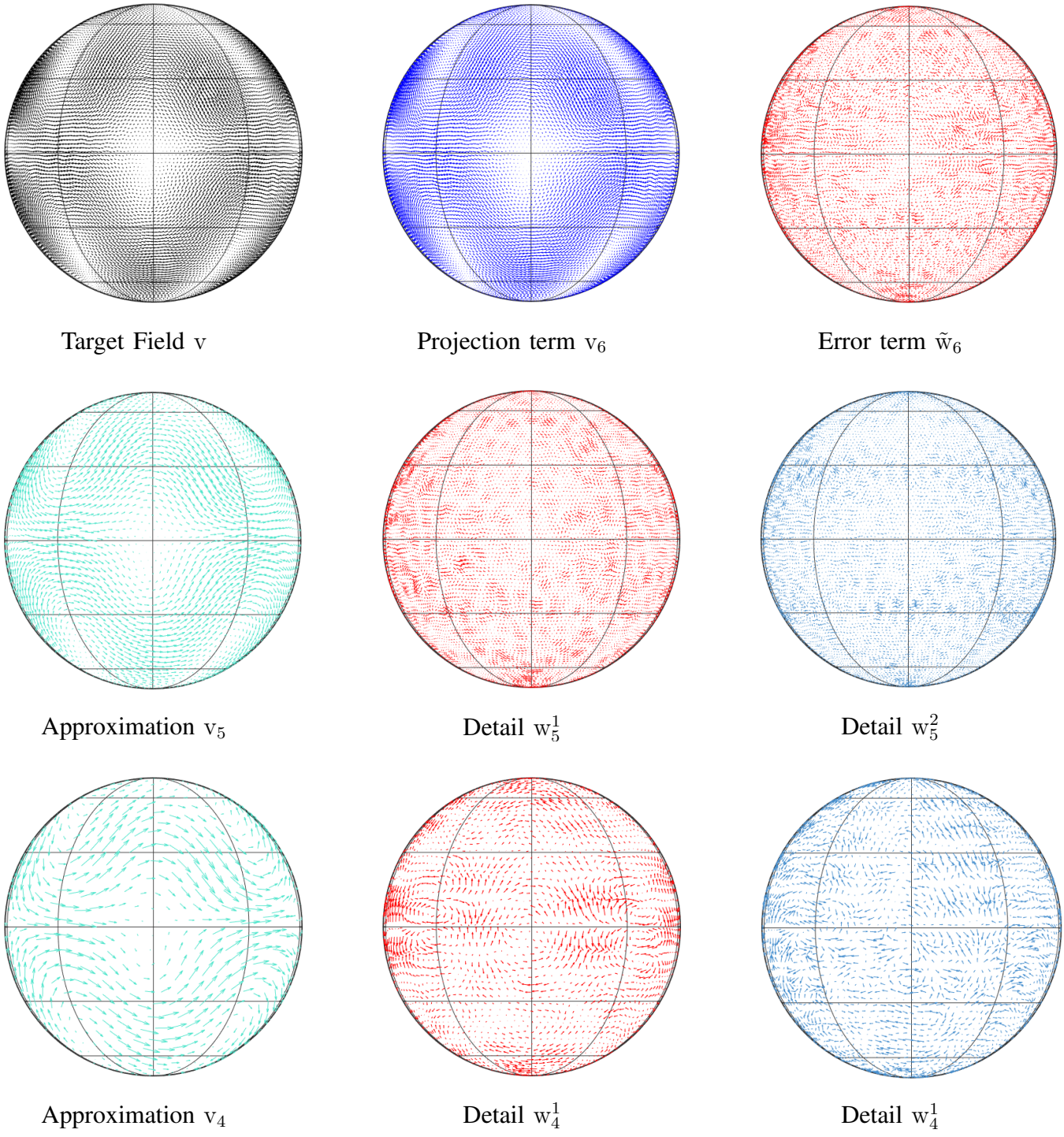

Fig. 4: Multiresolution decomposition of vector field 1 on GL rule $\mathcal{Q}_J$ with $J = 6$. The projection v_6 is decomposed to the downsampled low pass v_5 and two high passes w_5^1 and w_5^2 at level 5. The approximation term v_5 is decomposed to the low-pass and high-pass coefficients v_4, and w_4^1 and w_4^2 in the next coarser level 4. The reconstruction is the inverse process where the coarser-level low pass and high passes are upsampled to the low pass approximation in its finer level.

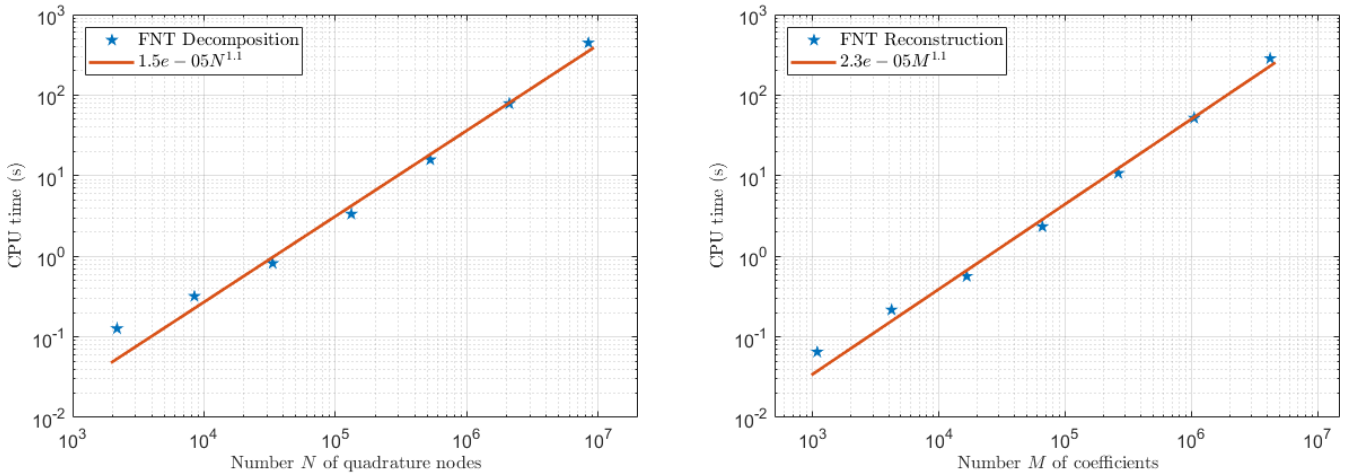

(a) Decomposition of Multi-Level FNT

(b) Reconstruction of Multi-Level FNT

Fig. 5: CPU time of FNT decomposition and FNT reconstruction.

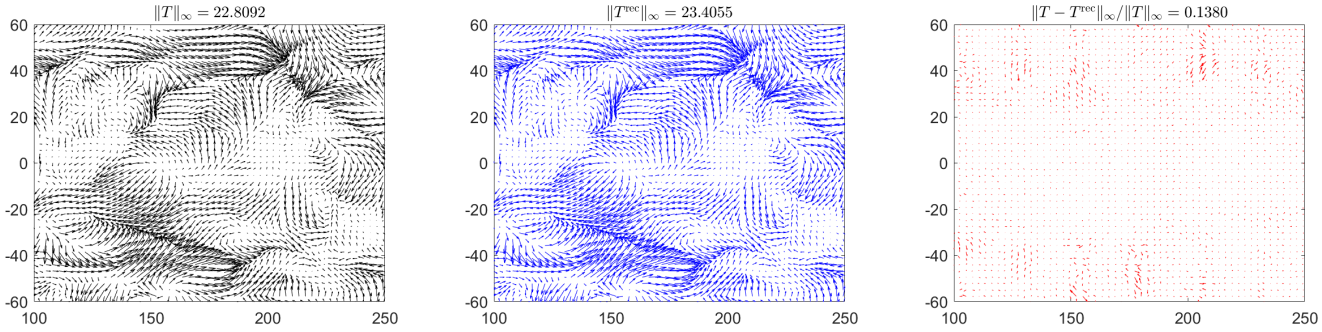

Fig. 6: Visualization of earth wind data reconstruction by one level FNT with GL points. The first plot shows the real wind field T while the second and third plots correspond to the reconstruction T^{rec} and the error $T - T^{\text{rec}}$, respectively. The normalized max norms for T, T^{rec}, and relative error $(T - T^{\text{rec}})/T$ are shown for each case.

REFERENCES

[1] W. Freeden and M. Schreiner, *Spherical Functions of Mathematical Geosciences: A Scalar, Vectorial, and Tensorial Setup*. Springer Science & Business Media, 2008.

[2] M. Ganesh, Q. T. Le Gia, and I. H. Sloan, "A pseudospectral quadrature method for navier-stokes equations on rotating spheres," *Mathematics of Computation*, pp. 1397–1430, 2011.

[3] F. Giraldo and T. Rosmond, "A scalable spectral element Eulerian atmospheric model (SEE-AM) for NWP: Dynamical core tests," *Monthly Weather Review*, vol. 132, pp. 133–153, 2004.

[4] J. R. Holton, "An introduction to dynamic meteorology," *American Journal of Physics*, vol. 41, no. 5, pp. 752–754, 1973.

[5] I. Watterson, "Decomposition of global ocean currents using a simple iterative method," *Journal of Atmospheric and Oceanic Technology*, vol. 18, no. 4, pp. 691–703, 2001.

[6] V. V. Anh, P. Broadbridge, A. Olenko, and Y. G. Wang, "On approximation for fractional stochastic partial differential equations on the sphere," *Stochastic Environmental Research and Risk Assessment*, vol. 32, no. 9, pp. 2585–2603, 2018.

[7] G. Wahba, "Vector splines on the sphere, with application to the estimation of vorticity and divergence from discrete, noisy data," in *Multivariate Approximation Theory II*. Springer, 1982, pp. 407–429.

[8] W. Freeden and T. Gervens, "Vector spherical spline interpolation–basic theory and computational aspects," *Mathematical Methods in the Applied Sciences*, vol. 16, no. 3, pp. 151–183, 1993.

[9] M. J. Fengler and W. Freeden, "A nonlinear Galerkin scheme involving vector and tensor spherical harmonics for solving the incompressible Navier–Stokes equation on the sphere," *SIAM Journal on Scientific Computing*, vol. 27, no. 3, pp. 967–994, 2005.

[10] T. N. Krishnamurti and L. Bounoua, *An Introduction to Numerical Weather Prediction Techniques*. CRC press, 2018.

[11] P. Lynch, "Deducing the wind from vorticity and divergence," *Monthly Weather Review*, vol. 116, no. 1, pp. 86–93, 1988.

[12] E. J. Fuselier and G. B. Wright, "Stability and error estimates for vector field interpolation and decomposition on the sphere with RBFs," *SIAM Journal on Numerical Analysis*, vol. 47, no. 5, pp. 3213–3239, 2009.

[13] B. G. Bodmann, G. Kutyniok, and X. Zhuang, "Gabor shearlets," *Applied and Computational Harmonic Analysis*, vol. 38, no. 1, pp. 87–114, 2015.

[14] E. Candes, L. Demanet, D. Donoho, and L. Ying, "Fast discrete curvelet transforms," *Multiscale Modeling and Simulation*, vol. 5, no. 3, pp. 861–899, 2006.

[15] C. K. Chui, *An Introduction to Wavelets*. Elsevier, 2016.

[16] A. Cohen, I. Daubechies, and P. Vial, "Wavelets on the interval and fast wavelet transforms," *Applied and Computational Harmonic Analysis*, 1993.

[17] I. Daubechies, *Ten lectures on wavelets*. SIAM, 1992, vol. 61.

[18] S. Mallat, *A Wavelet Tour of Signal Processing: The Sparce Way*. Elsevier, 2009.

[19] Y. Meyer, *Ondelettes et Opérateurs, Tomes I: Ondelettes*. Hermann, 1990.

[20] A. Ron and Z. Shen, "Affine systems in $L_2(\mathbf{R}^d)$: The analysis of the analysis operator," *Journal of Functional Analysis*, vol. 148, no. 2, pp. 408–447, 1997.

[21] I. Daubechies, B. Han, A. Ron, and Z. Shen, "Framelets: MRA-based constructions of wavelet frames," *Applied and Computational Harmonic Analysis*, vol. 14, no. 1, pp. 1–46, 2003.

[22] B. Han, Z. Zhao, and X. Zhuang, "Directional tensor product complex tight framelets with low redundancy," *Applied and Computational Harmonic Analysis*, vol. 41, no. 2, pp. 603–637, 2016.

[23] Y. G. Wang and X. Zhuang, "Tight framelets and fast framelet filter bank transforms on manifolds," *Applied and Computational Harmonic Analysis*, vol. https://doi.org/10.1016/j.acha.2018.02.001, 2018.

[24] B. Fischer and J. Prestin, "Wavelets based on orthogonal polynomials," *Mathematics of Computation of the American Mathematical Society*, vol. 66, no. 220, pp. 1593–1618, 1997.

[25] H. Mhaskar and J. Prestin, "Polynomial frames: a fast tour," *Approximation Theory XI: Gatlinburg*, pp. 101–132, 2004.

[26] R. R. Coifman and M. Maggioni, "Diffusion wavelets," *Applied and Computational Harmonic Analysis*, vol. 21, no. 1, pp. 53–94, 2006.

[27] B. Dong, "Sparse representation on graphs by tight wavelet frames and applications," *Applied and Computational Harmonic Analysis*, vol. 42, no. 3, pp. 452–479, 2017.

[28] M. Maggioni and H. Mhaskar, "Diffusion polynomial frames on metric measure spaces," *Applied and Computational Harmonic Analysis*, vol. 24, no. 3, pp. 329–353, 2008.

[29] H. Mhaskar, "Eignets for function approximation on manifolds," *Applied and Computational Harmonic Analysis*, vol. 29, no. 1, pp. 63–87, 2010.

[30] Q. T. Le Gia, M. Li, and Y. G. Wang, "FaVeST: Fast vector spherical harmonic transforms," *arXiv Preprint arxiv xxxx.xxxx*, 2019.

[31] B. Han and X. Zhuang, "Smooth affine shear tight frames with MRA structure," *Applied and Computational Harmonic Analysis*, vol. 39, no. 2, pp. 300–338, 2015.

[32] Q. T. Le Gia, I. H. Sloan, Y. G. Wang, and R. S. Womersley, "Needlet approximation for isotropic random fields on the sphere," *Journal of Approximation Theory*, vol. 216, pp. 86–116, 2017.

[33] Y. G. Wang, Q. T. Le Gia, I. H. Sloan, and R. S. Womersley, "Fully discrete needlet approximation on the sphere," *Applied and Computational Harmonic Analysis*, vol. 43, no. 2, pp. 292–316, 2017.

[34] A. R. Edmonds, *Angular Momentum in Quantum Mechanics*. Princeton University Press, 1996.

[35] L. C. Biedenharn and J. D. Louck, *Angular momentum in quantum physics: theory and application*. Cambridge University Press, 1984.

[36] P. Gordon, *Vorlesungen über Invariantentheorie*. Teubner, 1885, vol. 1.

[37] "NIST Digital Library of Mathematical Functions," http://dlmf.nist.gov/, Release 1.0.9 of 2014-08-29, 2014, online companion to [49].

[38] J. Keiner, S. Kunis, and D. Potts, "Efficient reconstruction of functions on the sphere from scattered data," *Journal of Fourier Analysis and Applications*, vol. 13, no. 4, pp. 435–458, 2007.

[39] V. Rokhlin and M. Tygert, "Fast algorithms for spherical harmonic expansions," *SIAM Journal on Scientific Computing*, vol. 27, no. 6, pp. 1903–1928, 2006.

[40] M. Tygert, "Fast algorithms for spherical harmonic expansions, II," *Journal of Computational Physics*, vol. 227, no. 8, pp. 4260–4279, 2008.

[41] ——, "Fast algorithms for spherical harmonic expansions, III," *Journal of Computational Physics*, vol. 229, no. 18, pp. 6181–6192, 2010.

[42] K. Hesse and R. S. Womersley, "Numerical integration with polynomial exactness over a spherical cap," *Advances in Computational Mathematics*, vol. 36, no. 3, pp. 451–483, 2012.

[43] R. S. Womersley, "Efficient spherical designs with good geometric properties," in *Contemporary Computational Mathematics-A Celebration of the 80th Birthday of Ian Sloan*. Springer. URL: https://web.maths.unsw.edu.au/~rsw/Sphere/, 2018, pp. 1243–1285.

[44] D. L. Williamson, J. B. Drake, J. J. Hack, R. Jakob, and P. N. Swarztrauber, "A standard test set for numerical approximations to the shallow water equations in spherical geometry," *Journal of Computational Physics*, vol. 102, no. 1, pp. 211–224, 1992.

[45] E. Kalnay, M. Kanamitsu, R. Kistler, W. Collins, D. Deaven, L. Gandin, M. Iredell, S. Saha, G. White, J. Woollen *et al.*, "The NCEP/NCAR 40-year reanalysis project," *Bulletin of the American Meteorological Society*, vol. 77, no. 3, pp. 437–472, 1996.

[46] R. Kistler, E. Kalnay, W. Collins, S. Saha, G. White, J. Woollen, M. Chelliah, W. Ebisuzaki, M. Kanamitsu, V. Kousky *et al.*, "The NCEP–NCAR 50-year reanalysis: monthly means CD-ROM and documentation," *Bulletin of the American Meteorological society*, vol. 82, no. 2, pp. 247–268, 2001.

[47] M. Kanamitsu, W. Ebisuzaki, J. Woollen, S.-K. Yang, J. Hnilo, M. Fiorino, and G. Potter, "NCEP·DOE AMIP-II Reanalysis (R-2)," *Bulletin of the American Meteorological Society*, vol. 83, no. 11, pp. 1631–1644, 2002.

[48] F. J. Narcowich, J. D. Ward, and G. B. Wright, "Divergence-free RBFs on surfaces," *Journal of Fourier Analysis and Applications*, vol. 13, no. 6, pp. 643–663, 2007.

[49] F. W. Olver, D. W. Lozier, R. F. Boisvert, and C. W. Clark, *NIST Handbook of Mathematical Functions Hardback and CD-ROM*. Cambridge University Press, 2010.